OUKA
The University of Osaka
Institutional Knowledge Archive

Title	Scaling of attraction force and rolling resistance in DEM with reduced particle stiffness
Author(s)	Washino, Kimiaki; Nakae, Shungo; Yamagami, Ryosuke et al.
Citation	Chemical Engineering Research and Design. 2024, 203, p. 501-519
Version Type	AM
URL	https://hdl.handle.net/11094/95385
rights	© 2024. This manuscript version is made available under the CC-BY-NC-ND 4.0 license https://creativecommons.org/licenses/by-nc-nd/4.0/
Note	

The University of Osaka Institutional Knowledge Archive : OUKA

https://ir.library.osaka-u.ac.jp/

The University of Osaka

Scaling of attraction force and rolling resistance in DEM with reduced particle stiffness

Kimiaki Washino*, Shungo Nakae, Ryosuke Yamagami, Ei L. Chan, Takuya Tsuji, Toshitsugu Tanaka

Department of Mechanical Engineering, Osaka University, Suita, Osaka 565-0871, Japan

Abstract

In Discrete Element Method (DEM), the stiffness of particles is often reduced artificially for calculation speed-up. It is known that the attraction force and rolling resistance should be scaled to counter-balance the excessive energy dissipation caused by prolonged contact duration with reduced stiffness. The present study theoretically derives the scaling laws from dimensionless equations of motion in a generic form, which are for both particle translation and rotation and with multi-body interactions. It is verified that the proposed scaling laws keep the same particle motion in the dimensionless time and space during the contact of more than two particles. It is also demonstrated that the behaviour of the original (stiff) particles in Couette flow can be replicated well in various conditions in general. Some deviation to the original system could be observed in certain conditions, which is likely related to the reduction of contact frequency.

*Corresponding author. Tel.: +81-6-6879-7318.
Email address: washino.k@mech.eng.osaka-u.ac.jp (Kimiaki Washino)

Keywords: DEM, Attraction force, Rolling resistance, Reduced particle stiffness, Calculation speed-up

1. Introduction

In the past decades, Discrete Element Method (DEM) [1] has been extensively used to simulate particulate flows. One of the most notable advantages of DEM over other modelling methods is that it can directly consider inter-particle interactions such as contact force, attraction force and rolling resistance. Both linear and non-linear spring-dashpot models are frequently used for the contact force [1, 2, 3, 4]. Typical attraction forces are the capillary force [5, 6, 7, 8], viscous force [9, 10, 11, 12, 13], electrostatic force [14, 15] and surface adhesion force [16, 17, 18, 19, 20]. Due to these forces, adhesive/cohesive particles can form agglomerates, lumps and/or wall make-ups, which are fundamentally different from free-flowing particles. Rolling resistance is used to express the rotational energy loss. It is needed to reproduce physical phenomena such as the formation of a shear band, which may not be observed with free-rolling particles. Physically speaking, rolling resistance can arise from various sources, e.g., micro-slip and friction on the contact surface, plastic deformation around the contact, viscous hysterisis and surface adhesion [21, 22, 23, 24]. In addition, rolling resistance is sometimes employed to artificially take into account the particle non-sphericity [25]. Many models for the rolling resistance are proposed in literature, and a good review and assessment of these models are provided by Ai et al. [26].

One of the existing challenges of DEM is the high computational cost to perform simulations with large number of particles. There are many approaches to speed-up DEM simulations, e.g., domain decomposition [27, 28], GPU computing [29, 30, 31], coarse grain model [32, 33, 34, 35, 36] and reduced particle stiffness [37, 38, 39, 40]. The reduced particle stiffness approach is particularly effective for stiff particles such as glass ballotini. In general, the time step interval for stable simulation is inversely proportional to the square-root of particle stiffness [2, 41]. Employing artificially reduced particle stiffness thus allows the use of a larger time step. When computational time per time step remains relatively constant, calculation speed scales directly with the increase in time step interval. Hereafter, the system with the original particle stiffness is called "original system", whilst that with reduced particle stiffness is called "reduced system".

For free-flowing particles, it is reported that the particle stiffness only has a limited impact on bulk particle behaviour [21, 37, 42, 43, 44, 45]. On the other hand, it is known that the particles in a reduced system can become more adhesive/cohesive than those in the original system when attraction forces are exerted on the particles [38]. This is due to the excessive energy dissipation associated with the attraction force during prolonged contact duration. There have been several attempts to scale the attraction forces so that this excessive energy dissipation can be counter-balanced [38, 39, 40, 46, 47].

Most, if not all, of such scaling laws for reduced particle stiffness are, however, derived from either the energy equation or equation of motion of

"two particles in contact", which does not guarantee the applicability in contact-dominant flow, i.e., the contact frequency of particles is high and the effect of multi-body contact is significant. Nevertheless, these scaling laws are used to simulate dense particle systems such as mixer flow and particle packing without a solid theoretical basis. The reduction of particle stiffness can also influence the rolling motion of particles, and scaling laws for rolling resistances may be necessary. However, the discussion of such scaling laws is still limited in literature and only available for specific combination of force and torque models [39, 40]. To the best of the authors' knowledge, generic scaling laws of rolling resistances are not yet proposed.

The present work is dedicated to developing scaling laws of attraction forces and rolling resistances that are derived from the dimensionless equations of motion in a generic form, which are for both particle translation and rotation and with multi-body interactions. The scaling laws are derived for both linear and non-linear contact models. This is an extended theory of the authors' previous work [46], which is named Reduced Particle Stiffness (RPS) scaling. Several test simulations are performed to assess the validity and applicability of the scaling laws.

2. Discrete Element Method

2.1. Governing equations

The translational and rotational equations of motion of Particle i interacting with adjacent Particles j are given as:

$$m_i \dot{\boldsymbol{v}}_i = \sum_j (\boldsymbol{F}_{Cij} + \boldsymbol{F}_{Aij}) \tag{1}$$

$$I_i \dot{\boldsymbol{\omega}}_i = \sum_j (\boldsymbol{M}_{Cij} + \boldsymbol{M}_{Aij} + \boldsymbol{M}_{Rij}) \tag{2}$$

where m is the particle mass, $\boldsymbol{v}$ is the particle velocity, I is the particle moment of inertia and $\boldsymbol{\omega}$ is the particle angular velocity. Only inter-particle forces and torques are considered in this work. $\boldsymbol{F}_C$ and $\boldsymbol{M}_C$ are the contact force and its torque, $\boldsymbol{F}_A$ and $\boldsymbol{M}_A$ are the attraction force and its torque and $\boldsymbol{M}_R$ is the rolling resistance. $\boldsymbol{M}_C$ and $\boldsymbol{M}_A$ are calculated as:

$$\boldsymbol{M}_C = r\boldsymbol{n} \times \boldsymbol{F}_C \tag{3}$$

$$\boldsymbol{M}_A = r\boldsymbol{n} \times \boldsymbol{F}_A \tag{4}$$

where r is the particle radius and $\boldsymbol{n}$ is the unit normal vector.

2.2. Contact force

Both linear and non-linear spring models are frequently used in DEM in literature [1, 2, 3, 4, 39]. In this section, both of the models are briefly summarised.

2.2.1. Linear spring-dashpot model

In the linear spring-dashpot model, the normal and tangential contact forces are expressed as:

$$\boldsymbol{F}_{C\mathrm{n}} = -(k_{\mathrm{n}}\delta_{\mathrm{n}} + \eta_{\mathrm{n}}\boldsymbol{v}_{rel}\cdot\boldsymbol{n})\boldsymbol{n} \tag{5}$$

$$\boldsymbol{F}_{C\mathrm{t}} = -\min[k_{\mathrm{t}}\delta_{\mathrm{t}} + \eta_{\mathrm{t}}v_s,\ \mu_s F_N]\boldsymbol{t} \tag{6}$$

where k is the spring constant, δ is the particle deformation (overlap), η is the damping coefficient, $\boldsymbol{v}_{rel}$ is the relative velocity, v_s is the magnitude of the relative tangential velocity at the contact surface, μ_s is the sliding friction coefficient and $\boldsymbol{t}$ is the unit tangent vector. The subscripts $_{\mathrm{n}}$ and $_{\mathrm{t}}$ indicate the normal and tangential directions, respectively. F_N is the normal load applied on the particle during sliding. The relative velocity is calculated as:

$$\boldsymbol{v}_{rel} = \boldsymbol{v}_i - \boldsymbol{v}_j \tag{7}$$

The restitution coefficient e is assumed to be constant when no force other than the contact force is acting on the particle. In this case, the damping coefficient can be determined as [2]:

$$\eta_{\mathrm{n}} = \sqrt{\frac{4m^* k_{\mathrm{n}}}{1 + (\pi/\ln(e))^2}} \tag{8}$$

where m^* is the reduced mass and given by:

$$\frac{1}{m^*} = \frac{1}{m_i} + \frac{1}{m_j} \tag{9}$$

The normal load during sliding, F_N, is given by the magnitude of the normal contact force.

2.2.2. Non-linear spring-dashpot model

The non-linear spring-dashpot models considered in this work are based on the Hertzian and JKR theories [3, 16]. The normal and tangential contact forces are given by:

$$\boldsymbol{F}_{C\mathrm{n}} = -\left(\frac{4E^*}{3r^*}a^3 + \eta_{\mathrm{n}}\boldsymbol{v}_{rel}\cdot\boldsymbol{n}\right)\boldsymbol{n} \tag{10}$$

$$\boldsymbol{F}_{C\mathrm{t}} = -\min[8G^*\sqrt{r^*\delta_{\mathrm{n}}}\delta_{\mathrm{t}} + \eta_{\mathrm{t}}v_s,\ \mu_s F_N]\boldsymbol{t} \tag{11}$$

where a is the contact radius and calculated differently in the Hertzian and JKR theories [48], and

$$\frac{1}{r^*} = \frac{1}{r_i} + \frac{1}{r_j} \tag{12}$$

$$\frac{1}{E^*} = \frac{1-\nu_i^2}{E_i} + \frac{1-\nu_j^2}{E_j} \tag{13}$$

$$\frac{1}{G^*} = \frac{2(2-\nu_i)(1+\nu_i)}{E_i} + \frac{2(2-\nu_j)(1+\nu_j)}{E_j} \tag{14}$$

where E is the Young's modulus and ν is the Poisson's ratio. The damping coefficients in the normal and tangential directions are given by [3]:

$$\eta_{\mathrm{n}} = -2\sqrt{\frac{5}{3}}\beta(m^* E^*)^{1/2} r^{*1/4} \delta_{\mathrm{n}}^{1/4} \tag{15}$$

$$\eta_{\mathrm{t}} = -4\sqrt{\frac{5}{3}}\beta(m^* G^*)^{1/2} r^{*1/4} \delta_{\mathrm{n}}^{1/4} \tag{16}$$

where β is a function of only the restitution coefficient and given by:

$$\beta = \frac{\ln(e)}{\sqrt{\ln^2(e) + \pi^2}} \tag{17}$$

F_N is given by the magnitude of the normal contact force when the Hertzian theory is used. In the JKR theory, it is replaced with the effective normal force [49, 50] as:

$$F_N = \left| 4\left(\frac{a}{a_0}\right)^3 - 4\left(\frac{a}{a_0}\right)^{3/2} + 2 \right| F_{po} \tag{18}$$

where F_{po} is the pull-off force and a_0 is the contact radius at the equilibrium condition, which are defined as:

$$F_{po} = 3\pi\gamma r^* \tag{19}$$

$$a_0 = \left(\frac{9\pi\gamma r^{*2}}{E^*}\right)^{1/3} \tag{20}$$

where γ is the surface energy of the particle.

2.3. Attraction force

In this section, the capillary, viscous and JKR surface adhesion forces that are used in Sections 4 and 5 are briefly summarised.

2.3.1. Capillary force model

Most of the capillary force models available in literature assume a symmetric pendular liquid bridge profile and do not consider the tangential force and torque arisen from asymmetry. The capillary force is written in a generic form as:

$$\boldsymbol{F}_{cap} = C_{cap}\boldsymbol{n} \tag{21}$$

where C_{cap} is a coefficient determined from the surface tension, liquid volume, particle size, contact angle and separation distance. For example, the Rabinovich-Lambert model [7, 8] gives the coefficient in the following form:

$$C_{cap} = \frac{4\pi r^* \sigma \cos\theta}{1 + 1/\left[\sqrt{1 + \dfrac{V_{liq}}{\pi r^* S^2}} - 1\right]} \tag{22}$$

where σ is the surface tension, V_{liq} is the liquid volume, θ is the contact angle and S is the inter-particle separation distance. A cut-off value, S_{min}, which is associated with the asperity of particle surface, is usually used to avoid S to be excessively small (or even negative during contact).

2.3.2. Viscous force model

The normal and tangential viscous forces are proportional to the relative velocity of the particles and can be written in a generic form as [51]:

$$\boldsymbol{F}_{v\mathrm{n}} = -C_N \boldsymbol{v}_{rel\mathrm{n}} \tag{23}$$

$$\boldsymbol{F}_{v\mathrm{t}} = -(C_T \boldsymbol{v}_{rel\mathrm{t}} + C_R \boldsymbol{\omega}_r \times \boldsymbol{n}) \tag{24}$$

where C_N, C_T and C_R are the damping coefficients related to the liquid viscosity, and

$$\boldsymbol{v}_{rel\mathrm{n}} = (\boldsymbol{v}_{rel} \cdot \boldsymbol{n})\boldsymbol{n} \tag{25}$$

$$\boldsymbol{v}_{rel\mathrm{t}} = \boldsymbol{v}_{rel} - \boldsymbol{v}_{rel\mathrm{n}} \tag{26}$$

$$\boldsymbol{\omega}_r = r_i \boldsymbol{\omega}_i + r_j \boldsymbol{\omega}_j \tag{27}$$

One may use the Adams & Perchard model [9] for C_N and the Goldman model [12] for C_T and C_R as:

$$C_N = \frac{6\pi\mu r^{*2}}{S} \tag{28}$$

$$C_T = 6\pi\mu r^* \left(\frac{8}{15} \ln\left(\frac{r^*}{S}\right) + 0.9588 \right) \tag{29}$$

$$C_R = \begin{cases} 6\pi\mu r^* \left(\dfrac{2}{15} \ln\left(\dfrac{r^*}{S}\right) - 0.2526) \right), & \text{if } S \ll 1 \\ \dfrac{6\pi\mu r^*}{8} \left(\dfrac{r^*}{S+r^*} \right)^4 \left(1 - \dfrac{3}{8} \dfrac{r^*}{S+r^*} \right), & \text{otherwise} \end{cases} \tag{30}$$

where μ is the liquid viscosity. A cut-off distance, S_{min}, is again used when evaluating these coefficients to prevent the resultant viscous forces from approaching infinity.

2.3.3. Surface adhesion force model

One of the most frequently used surface adhesion model in DEM is the JKR model [16]. It is generally acknowledged that this model is valid when the dimensionless Tabor parameter, λ_T given as follow, is large [52].

$$\lambda_T = \left(\frac{4r^* \gamma^2}{E^{*2} D_{min}^3} \right)^{1/3} \tag{31}$$

where D_{min} is the minimum atomic separation distance between the particles. In the JKR theory, the adhesion force is given by:

$$\boldsymbol{F}_{\mathrm{JKR}} = 4\sqrt{\pi \gamma E^* a^3}\boldsymbol{n} \tag{32}$$

It is noted that the adhesion force is proportional to $a^{3/2}$.

2.4. Rolling resistance

Many of the rolling resistance models used in DEM can be written in the following form:

$$\boldsymbol{M}_R = \chi_{sp}\boldsymbol{M}_{sp} + \chi_d \boldsymbol{M}_d + \chi_{sl}\boldsymbol{M}_{sl} \tag{33}$$

where $\boldsymbol{M}_{sp}$, $\boldsymbol{M}_d$ and $\boldsymbol{M}_{sl}$ are the torques due to the rotational spring, dashpot and slider, respectively, and χ_{sp}, χ_d and χ_{sl} are the corresponding mask

parameters which take either a value of zero or one to select the required components in each rolling resistance model. $\boldsymbol{M}_{sp}$, $\boldsymbol{M}_{d}$ and $\boldsymbol{M}_{sl}$ can be written in the following generic manner:

$$\boldsymbol{M}_{sp} = k_{roll}\boldsymbol{\theta}_{roll} \tag{34}$$

$$\boldsymbol{M}_{d} = \eta_{roll}\boldsymbol{\omega}_{roll} \tag{35}$$

$$\boldsymbol{M}_{sl} = M_{sl}\boldsymbol{e}_{roll} \tag{36}$$

where k_{roll} is the rolling spring stiffness, $\boldsymbol{\theta}_{roll}$ is the deformation (angle) vector of the rolling spring, η_{roll} is the rolling damping coefficient, $\boldsymbol{\omega}_{roll}$ is the directional angular velocity for the dashpot, M_{sl} is the magnitude of the rolling slider torque and $\boldsymbol{e}_{roll}$ is the unit direction vector for the slider. This section briefly summarises three different ways to evaluate Eqs. (34), (35) and (36), i.e., the Constant Directional Torque (CDT), Elastic-Plastic Spring-Dashpot (EPSD) and Adhesive Rolling (AR) models, which are used in Sections 4 and 5.

2.4.1. Constant directional torque model

The models in this category [21, 53] define the mask parameters as:

$$(\chi_{sp}, \chi_{d}, \chi_{sl}) = (0, 0, 1) \tag{37}$$

$\boldsymbol{M}_{sl}$ is a constant torque applied in the opposite direction of the relative angular velocity as:

$$M_{sl} = \mu_r r^* F_N \tag{38}$$

$$\boldsymbol{e}_{roll} = -\frac{\boldsymbol{\omega}_{rel}}{|\boldsymbol{\omega}_{rel}|} \tag{39}$$

$$\boldsymbol{\omega}_{rel} = \boldsymbol{\omega}_i - \boldsymbol{\omega}_j \tag{40}$$

where $\boldsymbol{\omega}_{rel}$ is the relative angular velocity and μ_r is the coefficient of rolling resistance which is dimensionless and defined as:

$$\mu_r = \tan \beta_r \tag{41}$$

where β_r is the angle of rolling resistance at which the rolling resistance counter-balances the torque due to gravity [26].

2.4.2. Elastic-plastic spring-dashpot model

The models in this category [22, 23] define the mask parameters as:

$$(\chi_{sp}, \chi_d, \chi_{sl}) = \begin{cases} (1,1,0), & \text{if } |\boldsymbol{M}_{sp}| < M_{sl} \\ (0,0,1), & \text{otherwise} \end{cases} \tag{42}$$

$\boldsymbol{M}_{sp}$ is calculated by integration from the beginning of contact (at $t = t_0$) as:

$$k_{roll}\boldsymbol{\theta}_{roll} = -\int_{t_0}^{t} k_r \boldsymbol{\omega}_{rel} d\tau \tag{43}$$

where k_r is defined as [26]:

$$k_r = 2.25 k_{\mathrm{n}} \mu_r^2 r^{*2} \tag{44}$$

Here, k_{n} is the spring constant in Eq. (5) for the linear model, or $k_{\mathrm{n}} = \frac{4}{3} E^* \sqrt{r^* \delta_{\mathrm{n}}}$ when the Hertzian model is used. $\boldsymbol{M}_d$ is given by:

$$\eta_{roll} = 2\eta_r \sqrt{I_r k_r} \tag{45}$$

$$\boldsymbol{\omega}_{roll} = -\boldsymbol{\omega}_{rel} \tag{46}$$

$$\frac{1}{I_r} = \frac{1}{I_i + m_i r_i^2} + \frac{1}{I_j + m_j r_j^2} \tag{47}$$

where η_r is a material dependant property. The magnitude of $\boldsymbol{M}_{sl}$ is the same as that of the CDT model (Eq. (38)) and the direction, $\boldsymbol{e}_{roll}$, is the same as that of $\boldsymbol{M}_{sp}$.

2.4.3. Adhesive rolling model

The models in this category [24, 54, 50, 55] (called AR model in this work) take into account the adhesive rolling behaviour in the JKR theory, and define the mask parameters as:

$$(\chi_{sp}, \chi_d, \chi_{sl}) = \begin{cases} (1,0,0), & \text{if } |\boldsymbol{M}_{sp}| < M_{sl} \\ (0,0,1), & \text{otherwise} \end{cases} \tag{48}$$

$\boldsymbol{M}_{sp}$ is caused by the asymmetric contact region and calculated as [24]:

$$k_{roll} = 4F_{po}r^* \left(\frac{a}{a_0}\right)^{3/2} \tag{49}$$

$$\boldsymbol{\theta}_{roll} = -\frac{1}{r^*}\left\{\left(\int_{t_0}^{t} \boldsymbol{v}_L d\tau\right) \cdot \boldsymbol{t}_r\right\}(\boldsymbol{t}_r \times \boldsymbol{n}) \tag{50}$$

$$\boldsymbol{v}_L = -r^* \boldsymbol{\omega}_{rel} \times \boldsymbol{n} \tag{51}$$

where $\boldsymbol{t}_r$ is the direction of the rolling velocity defined as:

$$\boldsymbol{t}_r = \frac{\boldsymbol{v}_L}{|\boldsymbol{v}_L|} \tag{52}$$

The magnitude of $\boldsymbol{M}_{sl}$ is given as:

$$M_{sl} = 4F_{po}r^* \left(\frac{a}{a_0}\right)^{3/2} \theta_{max} \tag{53}$$

where θ_{max} is the maximum rolling angle, which may be determined experimentally [56]. The direction vector, $\boldsymbol{e}_{roll}$, is the same as that of $\boldsymbol{M}_{sp}$.

2.5. Time step

In the linear spring-dashpot model, the time step is determined based on the theoretical oscillation period as [2]:

$$\Delta t \leq 2\pi f_l \sqrt{\frac{m}{k}} \tag{54}$$

where f_l is a safety factor which has to be small enough to resolve the oscillation. The time step for the non-linear spring-dashpot model is determined based on the Rayleigh time as [41]:

$$\Delta t \leq \frac{\pi f_{nl} r}{0.8766 + 0.163\nu} \sqrt{\frac{2\rho(1+\nu)}{E}} \tag{55}$$

The safety factor f_{nl} typically takes a value between 0.1 and 0.2.

The explicit velocity Verlet scheme [57] is employed for the numerical integration of the equations of motion in this work.

3. Scaling laws

As shown in Eqs. (54) and (55), the time step required in DEM is inversely-proportional to the square root of the particle stiffness. In many practical cases, the particle stiffness is therefore reduced artificially to speed-up the simulation. Washino et al. [46] proposed a generic scaling law for attraction force based on the dimensionless equations of motion. However, there are two limitations in the theory: only the normal (i.e., radial) motion is considered, and the equation of motion for binary collision is used. The authors applied the same scaling to oblique collisions and multi-body interactions without a solid theoretical basis. Moreover, a generic scaling law for rolling resistance is not yet proposed in literature.

This section explains an extended theory of the RPS scaling. Generic scaling laws for arbitrary attraction force and rolling resistance are derived

based on the dimensionless equations of motion that are (i) used for both normal and tangential motions (ii) with multi-body interactions and (iii) for translation and rotation.

3.1. Linear RPS scaling

3.1.1. Dimensionless governing equations

First, v_c, ω_c, k_c, r_c, m_c and I_c are chosen as characteristic velocity, angular velocity, spring constant, radius, mass and moment of inertia which represent the particles in a system of interest. Then, the dimensionless velocity, angular velocity, deformation, time, radius, mass and moment of inertia can be defined as follows:

$$\hat{\boldsymbol{v}} = \frac{\boldsymbol{v}}{v_c} \tag{56}$$

$$\hat{\boldsymbol{\omega}} = \frac{\boldsymbol{\omega}}{\omega_c} \tag{57}$$

$$\hat{\delta} = \frac{\delta}{v_c}\sqrt{\frac{k_c}{m_c}} \tag{58}$$

$$\hat{t} = t\sqrt{\frac{k_c}{m_c}} \tag{59}$$

$$\hat{r} = \frac{r}{r_c} \tag{60}$$

$$\hat{m} = \frac{m}{m_c} \tag{61}$$

$$\hat{I} = \frac{I}{I_c} \tag{62}$$

Using these dimensionless variables, Eqs. (1) and (2) are non-dimensionalised as follows:

$$\hat{m}_i \frac{d\hat{\boldsymbol{v}}_i}{d\hat{t}} = \sum_j (\hat{\boldsymbol{F}}_{Cij} + \hat{\boldsymbol{F}}_{Aij}) \tag{63}$$

$$\hat{I}_i \frac{d\hat{\boldsymbol{\omega}}_i}{d\hat{t}} = \sum_j (\hat{\boldsymbol{M}}_{Cij} + \hat{\boldsymbol{M}}_{Aij} + \hat{\boldsymbol{M}}_{Rij}) \tag{64}$$

The dimensionless contact forces in the normal and tangential directions are written as:

$$\hat{\boldsymbol{F}}_{C\mathrm{n}} = -\left(\hat{k}_{\mathrm{n}}\hat{\delta}_{\mathrm{n}} + \hat{\eta}_{\mathrm{n}}\hat{\boldsymbol{v}}_{rel}\cdot\boldsymbol{n}\right)\boldsymbol{n} \tag{65}$$

$$\hat{\boldsymbol{F}}_{C\mathrm{t}} = -\min\left[\hat{k}_{\mathrm{t}}\hat{\delta}_{\mathrm{t}} + \hat{\eta}_{\mathrm{t}}\hat{v}_s,\ \mu_s\hat{F}_N\right]\boldsymbol{t} \tag{66}$$

where

$$\hat{k}_{\mathrm{n}} = \frac{k_{\mathrm{n}}}{k_c} \tag{67}$$

$$\hat{k}_{\mathrm{t}} = \frac{k_{\mathrm{t}}}{k_c} \tag{68}$$

$$\hat{\eta}_{\mathrm{n}} = \sqrt{\frac{4\hat{m}^*\hat{k}_{\mathrm{n}}}{1+(\pi/\ln(e))^2}} \tag{69}$$

$$\hat{\eta}_{\mathrm{t}} = \sqrt{\frac{4\hat{m}^*\hat{k}_{\mathrm{t}}}{1+(\pi/\ln(e))^2}} \tag{70}$$

$$\hat{F}_N = |\hat{\boldsymbol{F}}_{C\mathrm{n}}| \tag{71}$$

The dimensionless attraction force is written as:

$$\hat{\boldsymbol{F}}_A = \frac{1}{v_c\sqrt{m_c k_c}}\boldsymbol{F}_A \tag{72}$$

The dimensionless torques due to the contact force, attraction force and rolling resistance are given as:

$$\hat{\boldsymbol{M}}_C = \frac{m_c v_c r_c}{I_c \omega_c} \hat{r}_i \boldsymbol{n} \times \hat{\boldsymbol{F}}_C \tag{73}$$

$$\hat{\boldsymbol{M}}_A = \frac{m_c v_c r_c}{I_c \omega_c} \hat{r}_i \boldsymbol{n} \times \hat{\boldsymbol{F}}_A \tag{74}$$

$$\hat{\boldsymbol{M}}_R = \frac{1}{I_c \omega_c} \sqrt{\frac{m_c}{k_c}} \boldsymbol{M}_R \tag{75}$$

The concept of the RPS scaling is to make all the dimensionless forces and torques to be the same between the original and reduced systems so that the dimensionless governing equations, Eqs (63) and (64), become identical. In the reduced system, all the characteristic quantities introduced above should be unchanged except for the spring constant, k_c. The reduction ratio Ω_k is defined as:

$$\Omega_k = k_{c\_\mathrm{R}} / k_{c\_\mathrm{O}} \tag{76}$$

where the subscripts $_{\_\mathrm{O}}$ and $_{\_\mathrm{R}}$ denote the properties in the original and reduced systems, respectively.

3.1.2. Contact force scaling

It is assumed that both $\hat{k}_\mathrm{n}$ and $\hat{k}_\mathrm{t}$ are the same between the original and reduced systems. This is a reasonable assumption since the reduction ratios for the normal stiffness and tangential stiffness are usually the same. Then, $\hat{\boldsymbol{F}}_C$ and $\hat{\boldsymbol{M}}_C$ in Eqs (65), (66) and (73) become identical between the

original and reduced systems since they do not contain k_c in the coefficient of each term, i.e., stiffness-independent. In other words, no scaling is required for the contact force and its torque. This is in line with the fact that the dynamic behaviours of free-flowing particles in many systems are not sensitive to particle stiffness [42, 43].

3.1.3. Attraction force scaling

The attraction force should be appropriately scaled to make $\hat{\boldsymbol{F}}_A$ in Eq. (72) the same between the original and reduced systems, that is:

$$\begin{aligned}\hat{\boldsymbol{F}}_{A\_\mathrm{O}} &= \frac{1}{v_c\sqrt{m_c k_{c\_\mathrm{O}}}}\boldsymbol{F}_{A\_\mathrm{O}} \\ &= \frac{1}{v_c\sqrt{m_c k_{c\_\mathrm{R}}}}\boldsymbol{F}_{A\_\mathrm{R}} \\ &= \hat{\boldsymbol{F}}_{A\_\mathrm{R}}\end{aligned} \tag{77}$$

This coincides with the original RPS scaling [46] and theoretically proves that the same scaling can be applied to both the normal and tangential attraction forces. The procedure to derive the scaling laws should vary depending on the form of $\boldsymbol{F}_A$, i.e., if it is or not a function of k and/or the variables which use k during the non-dimensionalisation (e.g. δ and t). More details about the procedure can be found in [46]. The scaling laws for the capillary and viscous forces expressed by Eqs. (21), (23) and (24) are listed in Table 1. As long as the attraction force is scaled, no special treatment is required for $\hat{\boldsymbol{M}}_A$ since it does not contain k_c in the coefficient of Eq. (74).

Table 1: Linear RPS scaling for attraction forces.

Type of force	Scaling law
Capillary force	$\boldsymbol{F}_{cap\_\mathrm{R}} = \sqrt{\Omega_k}\boldsymbol{F}_{cap\_\mathrm{O}}$
Normal viscous force	$\boldsymbol{F}_{v\mathrm{n}\_\mathrm{R}} = \sqrt{\Omega_k}\boldsymbol{F}_{v\mathrm{n}\_\mathrm{O}}$
Tangential viscous force	$\boldsymbol{F}_{v\mathrm{t}\_\mathrm{R}} = \sqrt{\Omega_k}\boldsymbol{F}_{v\mathrm{t}\_\mathrm{O}}$

3.1.4. Rolling resistance scaling

The rolling resistance should be scaled to make $\hat{\boldsymbol{M}}_R$ in Eq. (75) the same between the original and reduced systems:

$$\begin{aligned}\hat{\boldsymbol{M}}_{R\_\mathrm{O}} &= \frac{1}{I_c\omega_c}\sqrt{\frac{m_c}{k_{c\_\mathrm{O}}}}\boldsymbol{M}_{R\_\mathrm{O}} \\ &= \frac{1}{I_c\omega_c}\sqrt{\frac{m_c}{k_{c\_\mathrm{R}}}}\boldsymbol{M}_{R\_\mathrm{R}} \\ &= \hat{\boldsymbol{M}}_{R\_\mathrm{R}}\end{aligned} \tag{78}$$

As is the case for the attraction force in Section 3.1.3, the scaling laws vary depending on the form of $\boldsymbol{M}_R$. The scaling laws for the CDT and EPSD models are listed in Table 2. It is found that no scaling is required for the CDT and EPSD models. This agrees with the work by Miyai et al. [43] that used the rolling resistance model and found that the simulation results are not sensitive to the spring constant.

Table 2: Linear RPS scaling for rolling resistances.

Type of rolling resistance	Scaling law
CDT	$\boldsymbol{M}_{R\_\mathrm{R}} = \boldsymbol{M}_{R\_\mathrm{O}}$
EPSD	$\boldsymbol{M}_{R\_\mathrm{R}} = \boldsymbol{M}_{R\_\mathrm{O}}$

3.2. Non-linear RPS scaling

3.2.1. Dimensionless governing equations

The same procedure explained for the linear spring-dashpot model in Section 3.1 is reapplied to the non-linear spring-dashpot model. First, v_c, ω_c, E_c, r_c, m_c and I_c are chosen as characteristic velocity, angular velocity, Young's modulus, radius, mass and moment of inertia which represent the particles in a system of interest. The dimensionless velocity, angular velocity, deformation, contact radius, time, radius, mass and moment of inertia can then be defined as:

$$\hat{\boldsymbol{v}} = \frac{\boldsymbol{v}}{v_c} \tag{79}$$

$$\hat{\boldsymbol{\omega}} = \frac{\boldsymbol{\omega}}{\omega_c} \tag{80}$$

$$\hat{\delta} = \delta \left(\frac{E_c r_c^{1/2}}{m_c v_c^2} \right)^{2/5} \tag{81}$$

$$\hat{a} = a \left(\frac{E_c}{m_c v_c^2 r_c^2} \right)^{1/5} \tag{82}$$

$$\hat{t} = t \left(\frac{E_c r_c^{1/2} v_c^{1/2}}{m_c} \right)^{2/5} \tag{83}$$

$$\hat{r} = \frac{r}{r_c} \tag{84}$$

$$\hat{m} = \frac{m}{m_c} \tag{85}$$

$$\hat{I} = \frac{I}{I_c} \tag{86}$$

Using these dimensionless variables, Eqs. (1) and (2) are non-dimensionalised as follows:

$$\hat{m}_i \frac{d\hat{\boldsymbol{v}}_i}{d\hat{t}} = \sum_j (\hat{\boldsymbol{F}}_{Cij} + \hat{\boldsymbol{F}}_{Aij}) \tag{87}$$

$$\hat{I}_i \frac{d\hat{\boldsymbol{\omega}}_i}{d\hat{t}} = \sum_j (\hat{\boldsymbol{M}}_{Cij} + \hat{\boldsymbol{M}}_{Aij} + \hat{\boldsymbol{M}}_{Rij}) \tag{88}$$

The dimensionless contact forces in the normal and tangential directions are written as:

$$\hat{\boldsymbol{F}}_{C\mathrm{n}} = -\left(\frac{4\hat{E}^*}{3\hat{r}^*} \hat{a}^3 + \hat{\eta}_{\mathrm{n}} \hat{\boldsymbol{v}}_{rel} \cdot \boldsymbol{n} \right) \boldsymbol{n} \tag{89}$$

$$\hat{\boldsymbol{F}}_{C\mathrm{t}} = -\min[8\hat{G}^* \sqrt{\hat{r}^* \hat{\delta}_{\mathrm{n}}} \hat{\delta}_{\mathrm{t}} + \hat{\eta}_{\mathrm{t}} \hat{v}_s,\ \mu_s \hat{F}_N] \boldsymbol{t} \tag{90}$$

where

$$\hat{E}^* = \frac{E^*}{E_c} \tag{91}$$

$$\hat{G}^* = \frac{G^*}{E_c} \tag{92}$$

$$\hat{\eta}_{\mathrm{n}} = -2\sqrt{\frac{5}{3}} \beta (\hat{m}^* \hat{E}^*)^{1/2} \hat{r}^{*1/4} \hat{\delta}_{\mathrm{n}}^{1/4} \tag{93}$$

$$\hat{\eta}_{\mathrm{t}} = -4\sqrt{\frac{5}{3}} \beta (\hat{m}^* \hat{G}^*)^{1/2} \hat{r}^{*1/4} \hat{\delta}_{\mathrm{n}}^{1/4} \tag{94}$$

In the Hertzian theory, $\hat{F}_N$ is given by the magnitude of the normal contact force, that is:

$$\hat{F}_N = |\hat{\boldsymbol{F}}_{C\mathrm{n}}| \tag{95}$$

In the JKR theory, it is given by the effective normal force as:

$$\hat{F}_N = \left(\frac{r_c^2}{m_c^{3/2} v_c^3 E_c}\right)^{2/5} \left| 4\left(\frac{\hat{a}}{\hat{a}_0}\right)^3 - 4\left(\frac{\hat{a}}{\hat{a}_0}\right)^{3/2} + 2 \right| 3\pi\gamma\hat{r}^* \tag{96}$$

The dimensionless attraction force is written as:

$$\hat{\boldsymbol{F}}_A = \left(\frac{1}{m_c^{3/2} v_c^3 E_c r_c^{1/2}}\right)^{2/5} \boldsymbol{F}_A \tag{97}$$

The dimensionless torques due to the contact force, attraction force and rolling resistance are given as:

$$\hat{\boldsymbol{M}}_C = \frac{r_c m_c v_c}{I_c \omega_c} \hat{r} \boldsymbol{n} \times \hat{\boldsymbol{F}}_C \tag{98}$$

$$\hat{\boldsymbol{M}}_A = \frac{r_c m_c v_c}{I_c \omega_c} \hat{r} \boldsymbol{n} \times \hat{\boldsymbol{F}}_A \tag{99}$$

$$\hat{\boldsymbol{M}}_R = \frac{1}{I_c \omega_c} \left(\frac{m_c}{E_c r_c^{1/2} v_c^{1/2}}\right)^{2/5} \boldsymbol{M}_R \tag{100}$$

In the RPS scaling, all the dimensionless forces and torques need to be the same between the original and reduced systems so that the dimensionless governing equations, Eqs (87) and (88), become identical. In the reduced system, all the characteristic quantities introduced above should be unchanged except for the Young's modulus, E_c. The reduction ratio, Ω_E, is defined as:

$$\Omega_E = E_{c\_\mathrm{R}} / E_{c\_\mathrm{O}} \tag{101}$$

3.2.2. Contact force scaling

As long as $\hat{E}^*$ and $\hat{G}^*$ are kept the same between the original and reduced systems, $\hat{\boldsymbol{F}}_C$ and $\hat{\boldsymbol{M}}_C$ in Eqs. (89), (90) and (98) become identical since they do not contain E_c in the coefficient of each term when the Hertzian theory is used. This explains why Young's modulus has little impact on the dynamic behaviours of free-flowing particles as indicated by many papers in literature [21, 44, 37, 45]. The same applies to the JKR theory except that F_N needs to be scaled to compensate the change of $E_c^{-2/5}$ of the coefficient in Eq. (96). This is further discussed in the next section.

3.2.3. Attraction force scaling

The attraction force should be scaled to keep $\hat{\boldsymbol{F}}_A$ in Eq. (97) the same, i.e.:

$$\begin{aligned}\hat{\boldsymbol{F}}_{A\_\mathrm{O}} &= \left(\frac{1}{m_c^{3/2} v_c^3 E_{c\_\mathrm{O}} r_c^{1/2}}\right)^{2/5} \boldsymbol{F}_{A\_\mathrm{O}} \\ &= \left(\frac{1}{m_c^{3/2} v_c^3 E_{c\_\mathrm{R}} r_c^{1/2}}\right)^{2/5} \boldsymbol{F}_{A\_\mathrm{R}} \\ &= \hat{\boldsymbol{F}}_{A\_\mathrm{R}}\end{aligned} \tag{102}$$

The scaling for the capillary, viscous and JKR surface adhesion forces expressed by Eqs. (21), (23), (24) and (32) are listed in Table 3. Note that the scaling law for the surface energy of the JKR adhesion force is $\Omega^{2/5}$ and coincidentally the same as the others although the JKR adhesion force is a

function of a. This also agrees with the F_N scaling required in Eq. (96) as mentioned in Section 3.2.2. As long as $\hat{\boldsymbol{F}}_A$ is kept the same, the torque due to the attraction force in Eq. (99) does not require any treatment since it does not contain E_c in the coefficient.

Table 3: Non-linear RPS scaling for attraction forces.

Type of force	Scaling law
Capillary force	$\boldsymbol{F}_{cap\_\mathrm{R}} = \Omega_E^{2/5} \boldsymbol{F}_{cap\_\mathrm{O}}$
Normal viscous force	$\boldsymbol{F}_{v\mathrm{n}\_\mathrm{R}} = \Omega_E^{2/5} \boldsymbol{F}_{v\mathrm{n}\_\mathrm{O}}$
Tangential viscous force	$\boldsymbol{F}_{v\mathrm{t}\_\mathrm{R}} = \Omega_E^{2/5} \boldsymbol{F}_{v\mathrm{t}\_\mathrm{O}}$
JKR adhesion force	$\gamma_{\_\mathrm{R}} = \Omega_E^{2/5} \gamma_{\_\mathrm{O}}$

3.2.4. Rolling resistance scaling

The rolling resistance should be scaled to make $\hat{\boldsymbol{M}}_R$ in Eq. (100) the same between the original and reduced systems:

$$\begin{aligned} \hat{\boldsymbol{M}}_{R\_\mathrm{O}} &= \frac{1}{I_c \omega_c} \left(\frac{m_c}{E_{c\_\mathrm{O}} r_c^{1/2} v_c^{1/2}} \right)^{2/5} \boldsymbol{M}_{R\_\mathrm{O}} \\ &= \frac{1}{I_c \omega_c} \left(\frac{m_c}{E_{c\_\mathrm{R}} r_c^{1/2} v_c^{1/2}} \right)^{2/5} \boldsymbol{M}_{R\_\mathrm{R}} \\ &= \hat{\boldsymbol{M}}_{R\_\mathrm{R}} \end{aligned} \tag{103}$$

The scaling laws for the CDT, EPSD and AR models are listed in Table 4. It is important to mention that no scaling is required for the CDT and EPSD models since it provides theoretical justification for the first time to many pieces of work in literature that used these rolling resistance models with reduced Young's modulus [21, 44, 37, 45]. Note that $\gamma_{\_\mathrm{R}} = \Omega_E^{2/5} \gamma_{\_\mathrm{O}}$ and

$\theta_{max\_\mathrm{R}} = \Omega_E^{-2/5}\theta_{max\_\mathrm{O}}$ are also used in the AR model.

Table 4: Non-linear RPS scaling for rolling resistances.

Type of rolling resistance	Scaling law
CDT	$\boldsymbol{M}_{R\_\mathrm{R}} = \boldsymbol{M}_{R\_\mathrm{O}}$
EPSD	$\boldsymbol{M}_{R\_\mathrm{R}} = \boldsymbol{M}_{R\_\mathrm{O}}$
AR	$\boldsymbol{M}_{R\_\mathrm{R}} = \Omega_E^{2/5}\boldsymbol{M}_{R\_\mathrm{O}}$

4. Verification of dimensionless governing equations

In order to verify the RPS scaling laws summarised in Tables 1 to 4, which are derived from the dimensionless governing equations, the head-on collisions of three particles shown in Figure 1 are simulated. The particles are initially aligned in the y-direction. The top and middle particles initially move in the negative y-direction with a velocity of v_c, whilst the bottom particle moves in the positive y-direction with $2v_c$. The middle particle rotates in the z-direction with an initial angular velocity of ω_c. Due to the rotation, the particles also move in the x-direction after the collisions. Three cases (Cases 1, 2 and 3) with different combinations of contact forces, attraction forces and rolling resistance models are tested as shown in Table 5. The Rabinovich-Lambert model, Adams & Perchard model and Goldman model are used to calculate the coefficients of the capillary and viscous forces as explained in Sections 2.3.1 and 2.3.2. The forces and torques are exerted only when the particles are in contact, i.e., no negative overlap, to make it easier to assess the effect of the RPS scaling. In this way, the capillary and viscous forces are always evaluated using S_{min}, which is fixed to 0.05% of the

particle radius in these cases. Gravity is not considered in the simulations. The properties of the original particles in Cases 1 to 3 are shown in Tables 6 to 8, respectively.

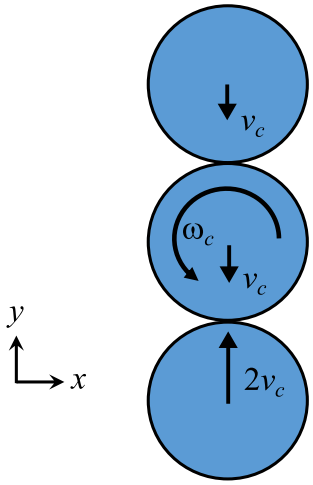

Figure 1: A schematic of head-on collisions of three particles.

Table 5: Models used for head-on collisions of three particles.

Case	Contact force	Attraction force	Rolling resistance
1	Linear	Capillary & viscous	EPSD
2	Non-linear (Hertz)	Capillary & viscous	CDT
3	Non-linear (JKR)	JKR	AR

First, we prove that the rolling resistance has a visible impact on the behaviour of the original particles with the calculation conditions used. Figures 2 to 4 show the dimensionless velocities of the middle particle with and without rolling resistance, as a function of the dimensionless time in Cases 1 to 3, respectively, where (a) is the normal velocity (i.e., the y-direction), (b) is the tangential velocity (i.e., the x-direction) and (c) is the angular velocity.

Table 6: Properties of original system for head-on collisions of three particles (Case 1).

Property	Value
Particle diameter d [mm]	1
Particle density ρ [kg/m^3]	2500
Spring constant k_n, k_t [N/m]	8.1×10^4
Coefficient of restitution e [-]	0.9
Sliding friction coefficient μ_s [-]	0.3
Rolling friction coefficient μ_r [-]	0.5
Rolling damping coefficient η_r [-]	0.1
Surface tension σ [N/m]	0.07
Contact angle θ [rad]	0
Liquid viscosity μ [Pa $\cdot$ s]	0.001
Liquid bridge volume V_{liq} [mm^3]	2.18×10^{-3}
Impact velocity v_c [m/s]	0.001
Initial angular velocity ω_c [rad/s]	10

Table 7: Properties of original system for head-on collisions of three particles (Case 2).

Property	Value
Particle diameter d [mm]	1
Particle density ρ [kg/m^3]	2500
Young's modulus E [GPa]	10
Coefficient of restitution e [-]	0.9
Poisson's ratio ν [-]	0.25
Sliding friction coefficient μ_s [-]	0.3
Rolling friction coefficient μ_r [-]	0.1
Surface tension σ [N/m]	0.07
Contact angle θ [rad]	0
Liquid viscosity μ [Pa $\cdot$ s]	0.001
Liquid bridge volume V_{liq} [mm^3]	2.18×10^{-3}
Impact velocity v_c [m/s]	0.001
Initial angular velocity ω_c [rad/s]	10

Table 8: Properties of original system for head-on collisions of three particles (Case 3).

Property	Value
Particle diameter d [μm]	1
Particle density ρ [kg/m^3]	2500
Young's modulus E [GPa]	10
Coefficient of restitution e [-]	0.9
Poisson's ratio ν [-]	0.25
Sliding friction coefficient μ_s [-]	0.3
Surface energy γ [J/m^2]	0.1
Maximum rotation angle θ_{max} [rad]	0.01
Impact velocity v_c [m/s]	0.3
Initial angular velocity ω_c [rad/s]	1

In all cases, it is observed that the rolling resistance has almost no impact on the normal velocity but largely influences the angular velocity. It can also be seen that the rolling resistance can have a non-negligible impact on the tangential velocity.

Three simulations are performed in each case using (i) original particle stiffness, (ii) reduced particle stiffness with the RPS scaling and (iii) reduced particle stiffness without any scaling. The particle stiffness is reduced by 100 times, i.e., $\Omega_k = \Omega_E = 10^{-2}$. The time step is determined based on the criteria explained in Section 2.5 to ensure stable solution of the equations of motion in all cases. Figures 5 to 7 show the change of the dimensionless (a) normal velocity, (b) tangential velocity and (c) angular velocity of the middle particle with respect to the dimensionless time in Cases 1 to 3, respectively. It can be clearly seen that reduced particle stiffness with the RPS scaling can provide the same curves as those of the original stiffness in all cases. On

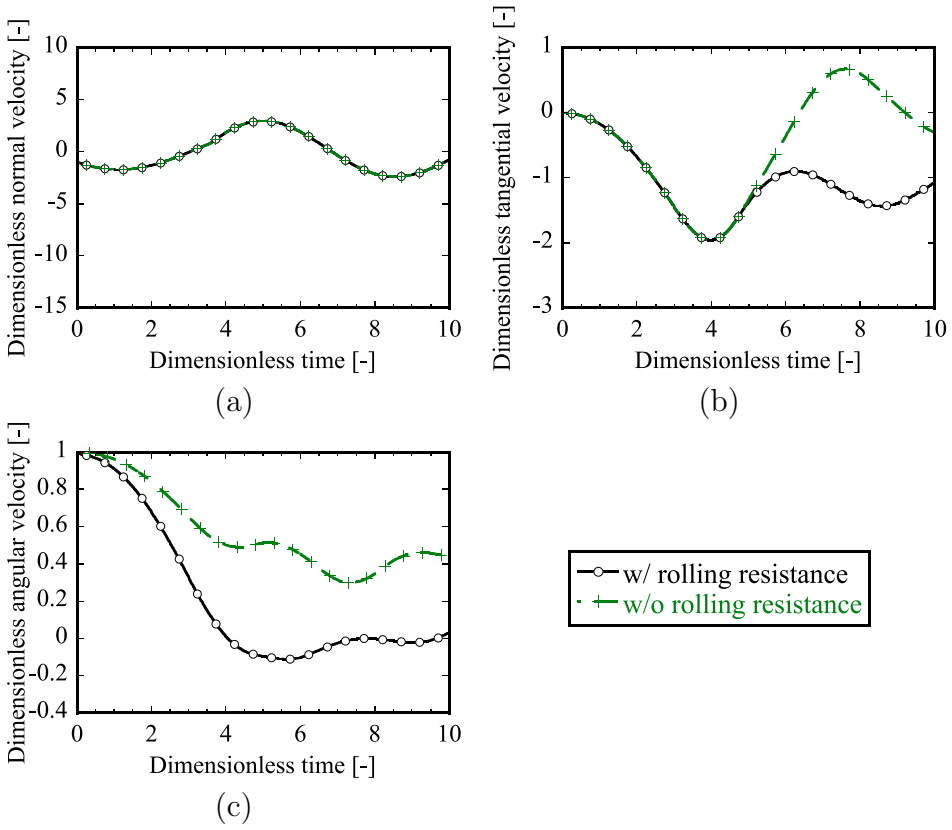

Figure 2: Change of dimensionless (a) normal velocity, (b) tangential velocity and (c) angular velocity of original particle in the middle with respect to dimensionless time with and without rolling resistance (Case 1).

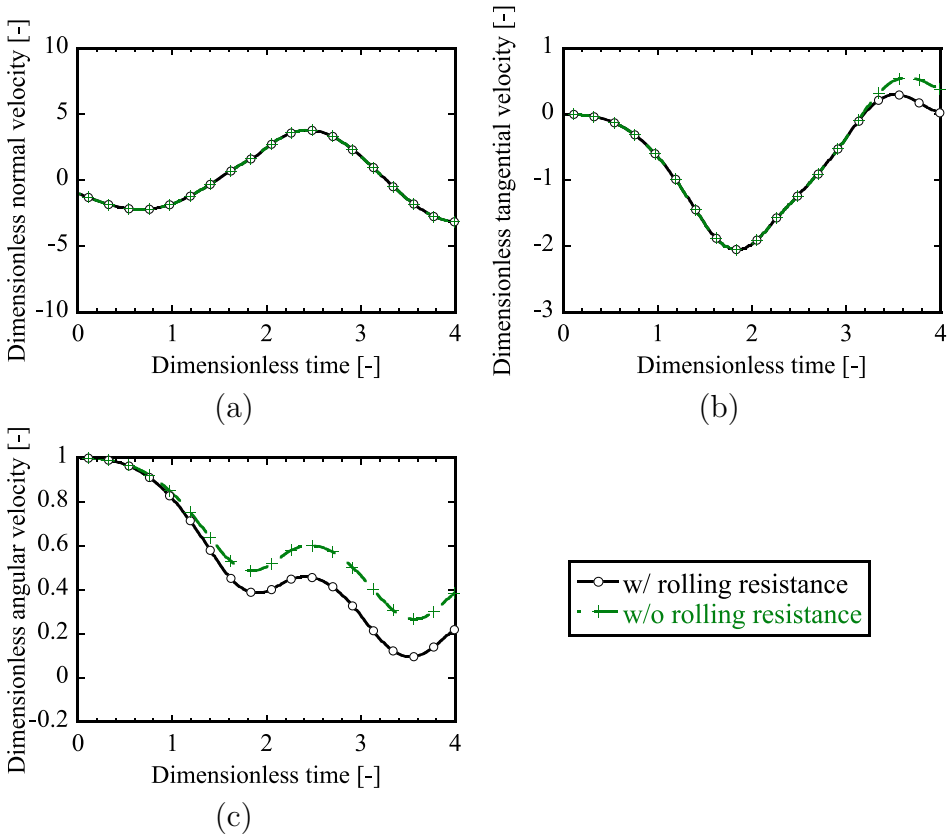

Figure 3: Change of dimensionless (a) normal velocity, (b) tangential velocity and (c) angular velocity of original particle in the middle with respect to dimensionless time with and without rolling resistance (Case 2).

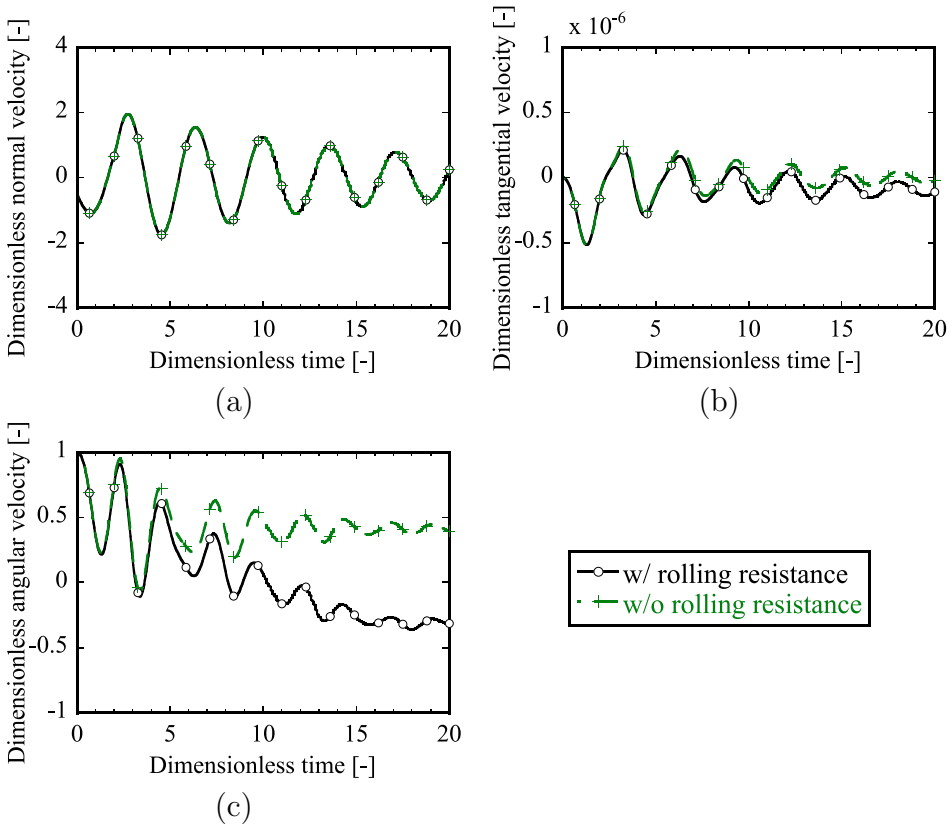

Figure 4: Change of dimensionless (a) normal velocity, (b) tangential velocity and (c) angular velocity of original particle in the middle with respect to dimensionless time with and without rolling resistance (Case 3).

the other hand, the reduced particle stiffness without any scaling tends to give larger velocity fluctuations, which can lead to larger energy dissipation with time. These results verify that the RPS scaling can maintain the same movement of the particles in the dimensionless time and space during contact with any combination of contact force, attraction force and rolling resistance models since it considers multi-body interactions in the both normal and tangential directions. This is not guaranteed theoretically in the authors' previous work [46] nor any other work in literature which uses a binary system for the derivation [38, 39, 47, 40].

5. Validation of RPS scaling

Simulations of Couette flows are presented in this section to discuss the validity of the RPS scaling in various conditions; with different particle volume fraction and reduction ratio (Section 5.1), mass ratio of large and small particles (Section 5.2) and rolling resistance models (Section 5.3). The simulation domain is $100 \times 10 \times 100$ mm^3 in the x, y and z directions, respectively. Two parallel walls are placed at $z = 0$ and 100 mm, which move in the opposite x directions with a constant speed of 2 m/s. Periodic boundaries are employed in the both x and y directions. The particle angular velocity is set to zero upon contact with the moving walls, and significantly high μ_s such as 10 is employed between the particles and walls. This enforces the no-slip condition at the particle surface as well as the particle centroid, which is a combination of Type A and B boundary conditions in [58]. Gravity is not

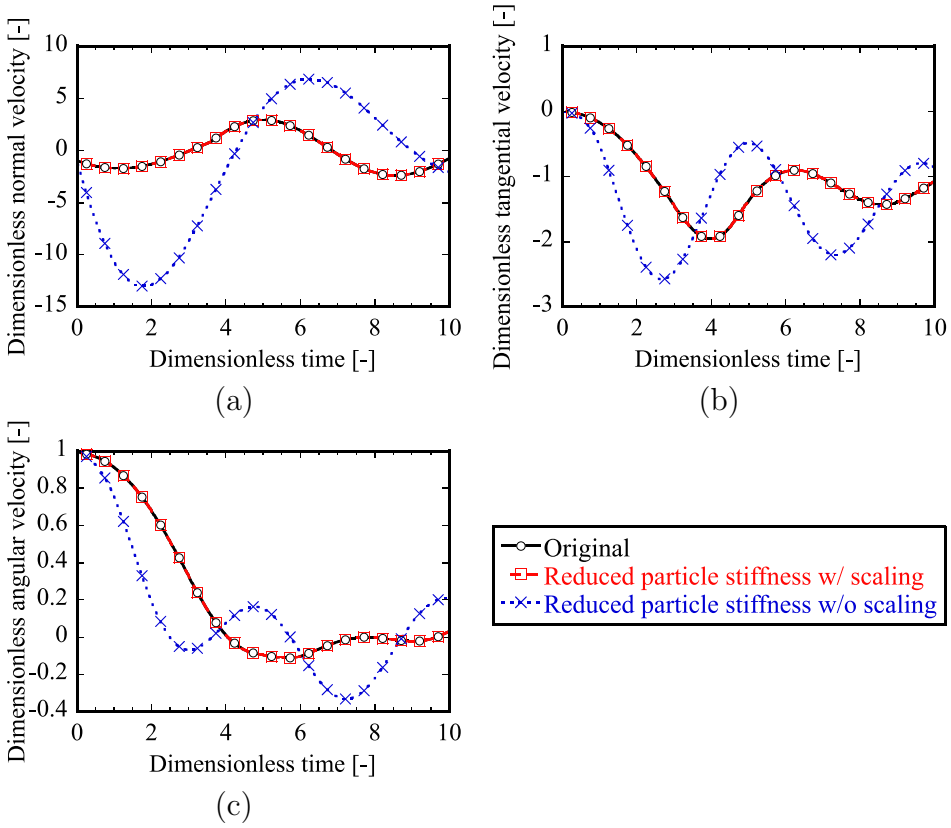

Figure 5: Change of dimensionless (a) normal velocity, (b) tangential velocity and (c) angular velocity with respect to dimensionless time with (Case 1). $\Omega_k = 10^{-2}$ is used for reduced system.

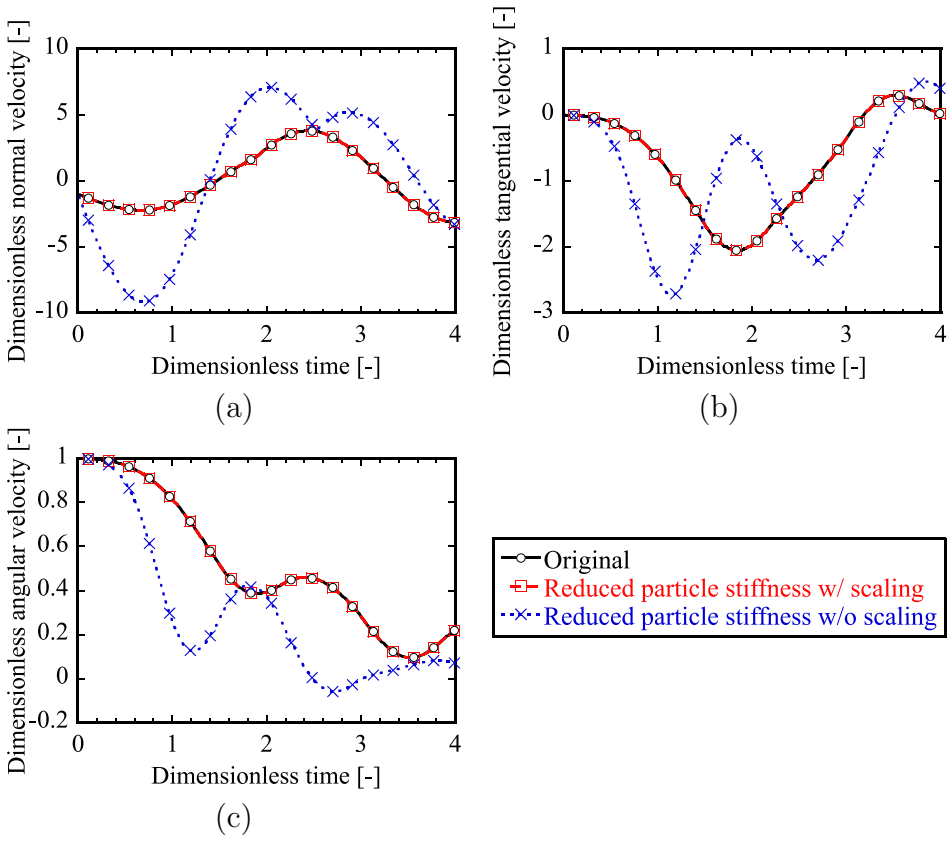

Figure 6: Change of dimensionless (a) normal velocity, (b) tangential velocity and (c) angular velocity with respect to dimensionless time (Case 2). $\Omega_E = 10^{-2}$ is used for reduced system.

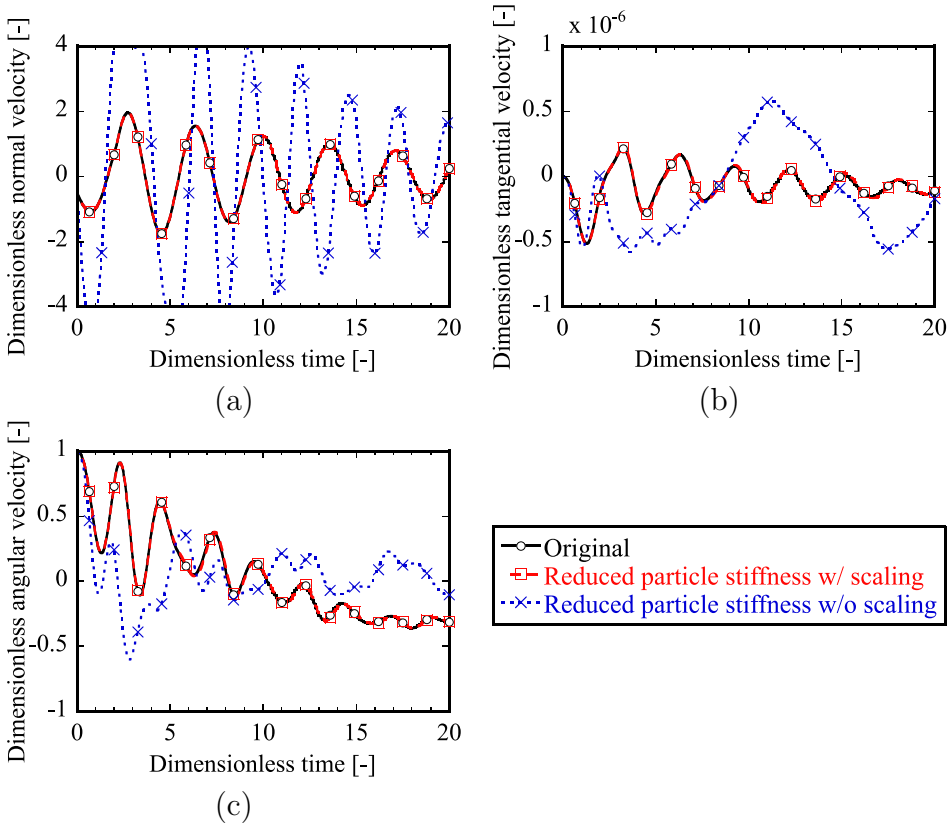

Figure 7: Change of dimensionless (a) normal velocity, (b) tangential velocity and (c) angular velocity with respect to dimensionless time (Case 3). $\Omega_E = 10^{-2}$ is used for reduced system.

considered in the simulations.

The common properties of the original particles are listed in Table 9. Simulations with the original and reduced particle stiffness are performed in each case to compare the results. The time step is determined based on the criteria explained in Section 2.5 to ensure stable solution of the equations of motion in all cases. The particles are generated in the simulation domain until the volume fraction reaches the target value. The x component of the initial particle velocity follows the ideal linear profile of the Couette flow, whilst the other components are randomly assigned between 0 and 0.1 m/s.

The simulations are continued for 100 seconds after steady state is reached. The results in steady state are then analysed to obtain the profiles of time- and spatial-averaged quantities such as the velocity, volume fraction, granular temperature and rotational energy within the sub-domains with a height of Δz. The granular temperature, T, is defined as:

$$T = \frac{1}{3N} \left(\sum_{k=1}^{3} \sum_{i=1}^{N} \left(v_{k,i} - \langle v_k \rangle_i \right)^2 \right) \tag{104}$$

where N is the number of particles within the sub-domain, $k = 1$, 2 and 3 stand for the x, y and z directions, respectively, and $\langle v \rangle$ is the average velocity. Note that $\langle v_k \rangle_i$ indicates that the average velocity is calculated per particle between $z_i - \Delta z/2$ and $z_i + \Delta z/2$ (rather than using the average velocity in the sub-domain) so that the granular temperature is not sensitive to Δz.

Table 9: Common properties of original particles for Couette flow.

Property	Value
Particle density ρ [kg/m^3]	2500
Young's modulus E [GPa]	10
Coefficient of restitution e [-]	0.81
Poisson's ratio ν [-]	0.25
Sliding friction coefficient μ_s [-]	0.3

5.1. Dilute and dense flows

Simulations are performed with different particle volume fractions, ϕ, between 0.1 and 0.5 as shown in Figure 8. The particle diameter is given with the Gaussian distribution with a mean of 1 mm and standard deviation of 0.05 mm. This small size distribution can avoid the potential formation of crystallised structures. The JKR and AR models are employed for the attraction force and rolling resistance, respectively, with a surface energy of 0.02 J/m^2 and maximum rotation angle of 0.01 rad. The surface energy used is not so high that the particles do not form large agglomerates or lumps, and yet it has an impact on the flow as discussed below. In the reduced system, the Young's modulus is reduced by 100 and 10000 (i.e., $\Omega_E = 10^{-2}$ and 10^{-4}).

Figure 9 shows the profiles of the aforementioned quantities of the original particles in a relatively dilute case ($\phi = 0.1$). The results with $\gamma = 0$ J/m^2 are also plotted to see the influence of the attraction force and rolling resistance. The distance from the bottom wall is normalised with the gap between the top and bottom walls, H. In Figure 9a, it can be seen that the profile of the average velocity is almost perfectly linear, and no-slip boundary condition is

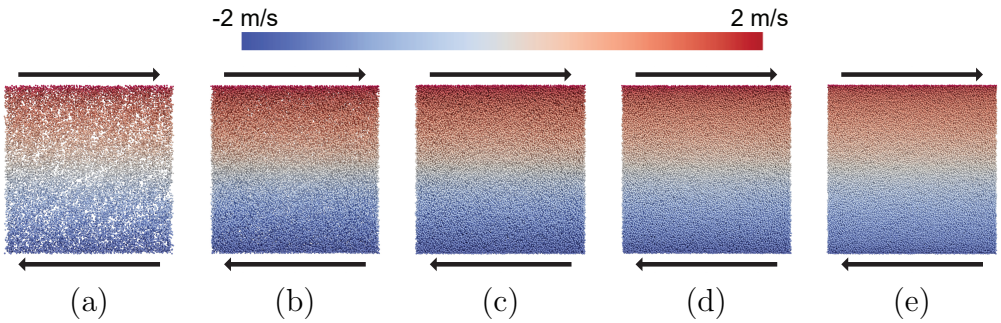

Figure 8: Snapshots of Couette flow of original particles with volume fraction of (a) 0.1, (b) 0.2, (c) 0.3, (d) 0.4 and (e) 0.5. The colour indicates the particle velocity in the shear (i.e., x) direction.

met at the walls. It is often reported in literature that the volume fraction near flat walls can drop due to the geometrical constraint, that is referred to as the wall effect [58]. However, in Figure 9b, it actually increases because of the large energy dissipation per collision caused by the forceful removal of the particle rotation upon contact with the walls. The large energy dissipation also leads to the drop of the granular temperature and rotational energy in Figure 9c and 9d. Comparing the results of $\gamma = 0.02$ and 0 J/m^2, it can be said that the surface energy does not affect the profiles of the average velocity and volume fraction, but has a noticeable decrease of the granular temperature and rotational energy by approximately 5%.

Figure 10 shows the results of the original particles in a relatively dense case ($\phi = 0.4$). A linear velocity profile can be observed again albeit a very subtle deviation near the walls. The volume fraction decreases in the regions $z/H < 0.2$ and $z/H > 0.8$ whilst the granular temperature and rotational energy increase due to the wall effect in contrast to the dilute case in Figure

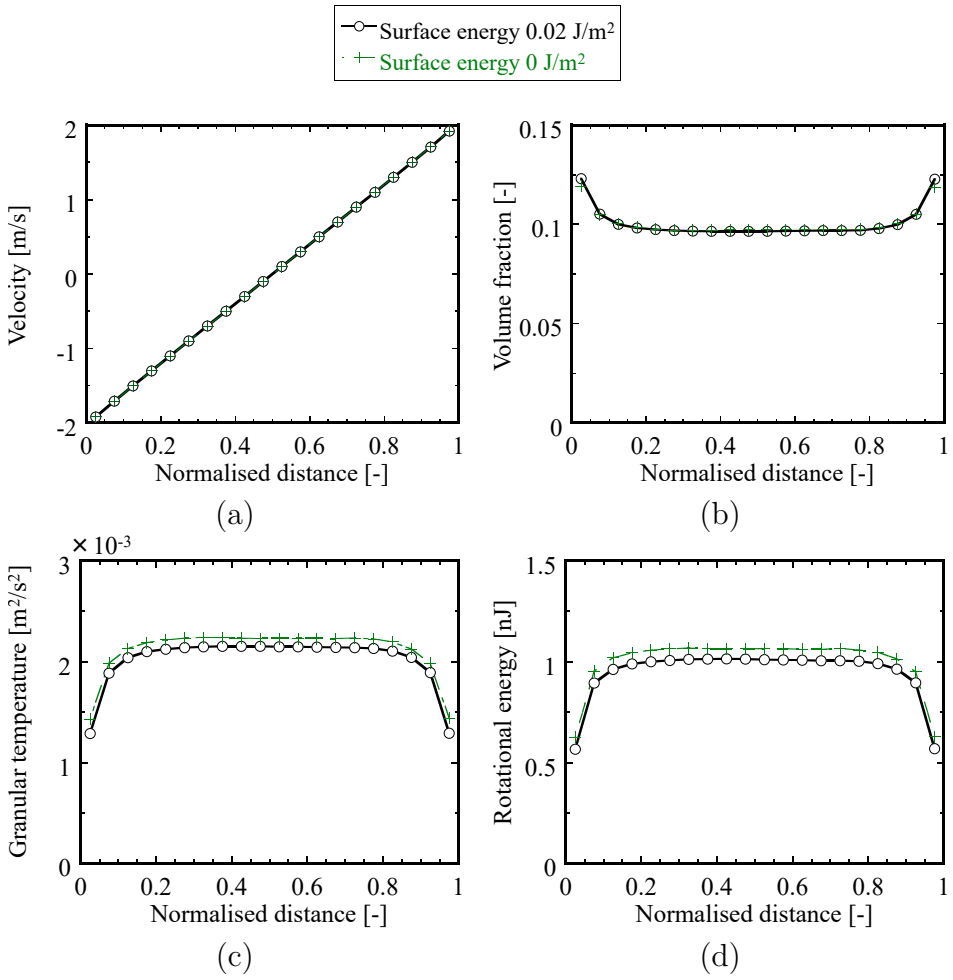

Figure 9: Profiles of time- and spatial-averaged quantities in original system; (a) velocity, (b) volume fraction, (c) granular temperature and (d) rotational energy in steady state ($\phi = 0.1$). The distance is normalised with the gap between the top and bottom walls.

9. The surface energy does not change the average velocity and volume fraction but has a clearer impact on the granular temperature and rotational energy (decrease by more than 10%). Note that the granular temperature and rotational energy are much lower than those with $\phi = 0.1$ due to the increased volume fraction and hence, higher contact frequency.

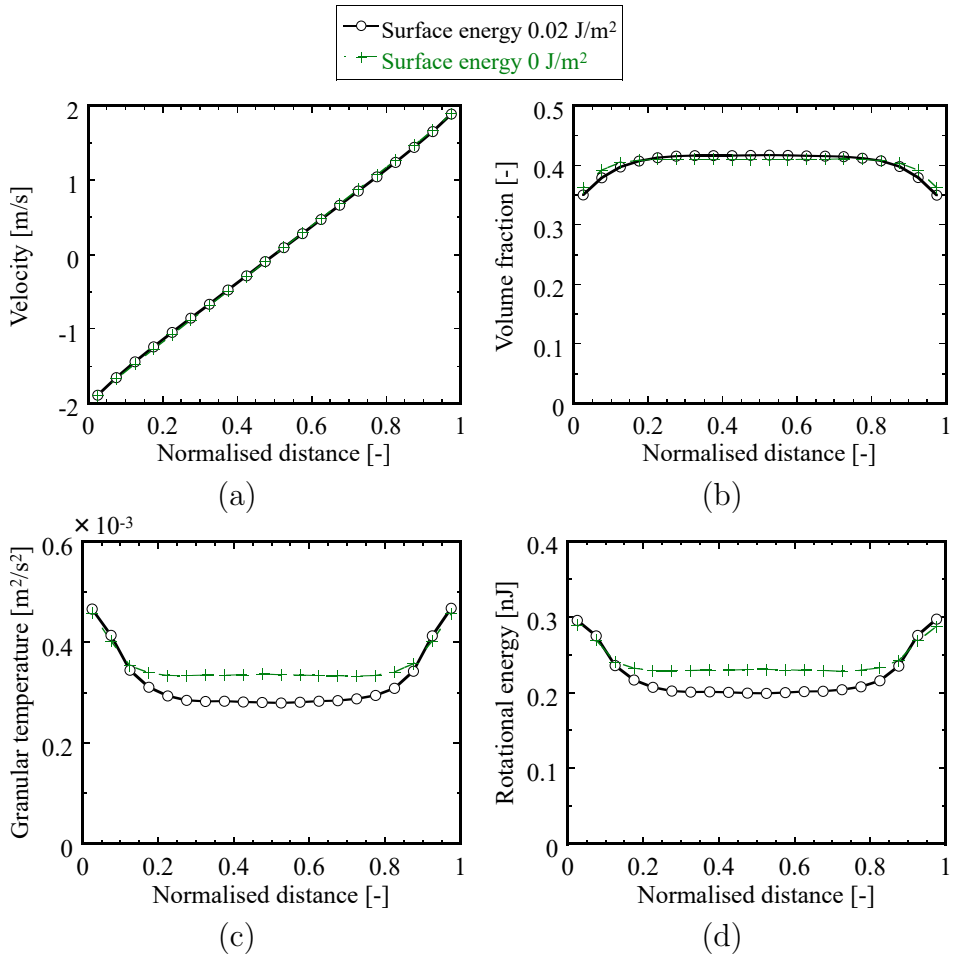

Figure 10: Profiles of time- and spatial-averaged quantities in original system; (a) velocity, (b) volume fraction, (c) granular temperature and (d) rotational energy in steady state ($\phi = 0.4$). The distance is normalised with the gap between the top and bottom walls.

Figures 11 and 12 show the results of the original and reduced systems with $\phi = 0.1$ and 0.4, respectively, with $\Omega_E = 10^{-2}$ and 10^{-4}. When $\Omega_E = 10^{-2}$, it can be seen that the results with the RPS scaling are in good agreement with those of the original systems. As expected, the results are largely different when the particle stiffness is simply reduced without any scaling especially with $\phi = 0.4$ because of the formation of large agglomerates as reflected by the volume fraction fluctuation in Figure 12b. This is in line with the observations in literature [38, 40] where simple reduction of particle stiffness makes the particles more "cohesive".

When $\Omega_E = 10^{-4}$, the results with the RPS scaling are still in good agreement with those of the original system in Figure 11c and 11d, but some visible deviation can be seen in Figure 12c and 12d. Figure 13 shows the granular temperature and rotational energy averaged between $z/H = 0.2$ and 0.8 and normalised with the results of the original system. It is clear that the deviation increases as ϕ increases or Ω_E decreases after a certain critical value. The deviation is particularly large in the following three conditions: (1) $\phi = 0.4$ and $\Omega_E = 10^{-4}$, (2) $\phi = 0.5$ and $\Omega_E = 10^{-2}$ and (3) $\phi = 0.5$ and $\Omega_E = 10^{-4}$. The cause of this discrepancy is still unknown and an open question. For example, He et al. [40] argued that the discrepancy may be related to the difference of the tangential displacement during contact. Another possible reason is that the contact frequency may be reduced due to the prolonged contact duration. Even if the RPS scaling maintains the energy dissipation per collision, the total energy dissipation can be small if

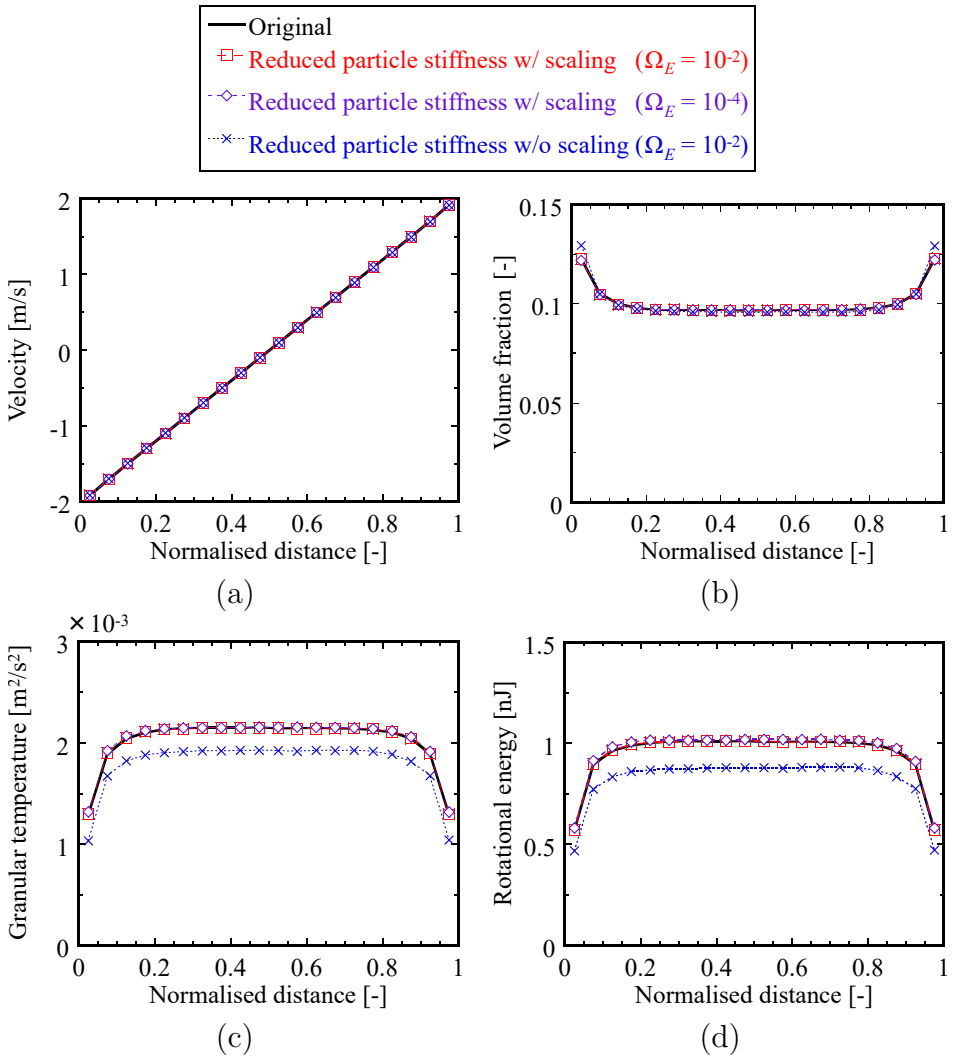

Figure 11: Profiles of time- and spatial-averaged quantities in original and reduced systems; (a) velocity, (b) volume fraction, (c) granular temperature and (d) rotational energy in steady state ($\phi = 0.1$).

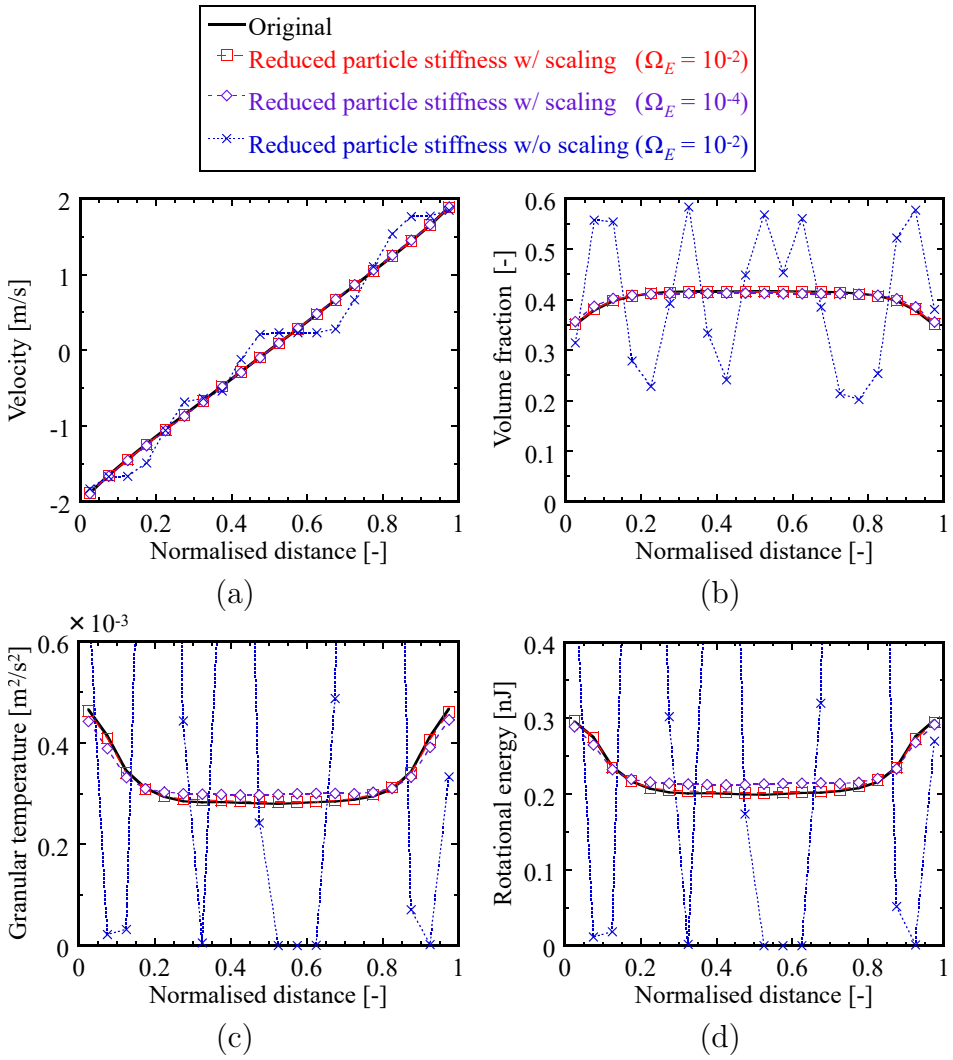

Figure 12: Profiles of time- and spatial-averaged quantities in original and reduced systems; (a) velocity, (b) volume fraction, (c) granular temperature and (d) rotational energy in steady state ($\phi = 0.4$).

the contact frequency is small. Figure 14 shows the average contact (collision) frequency computed between $z/H = 0.2$ and 0.8. Strong correlation can be observed between the deviation of contact frequency from the original system and that of the granular temperature and rotational energy, particularly in the aforementioned three conditions of ϕ and Ω_E. This implies that the application range of the RPS scaling may be expanded if the deviation of contact frequency is corrected. However, it is beyond the scope of the present study and will be discussed in future work.

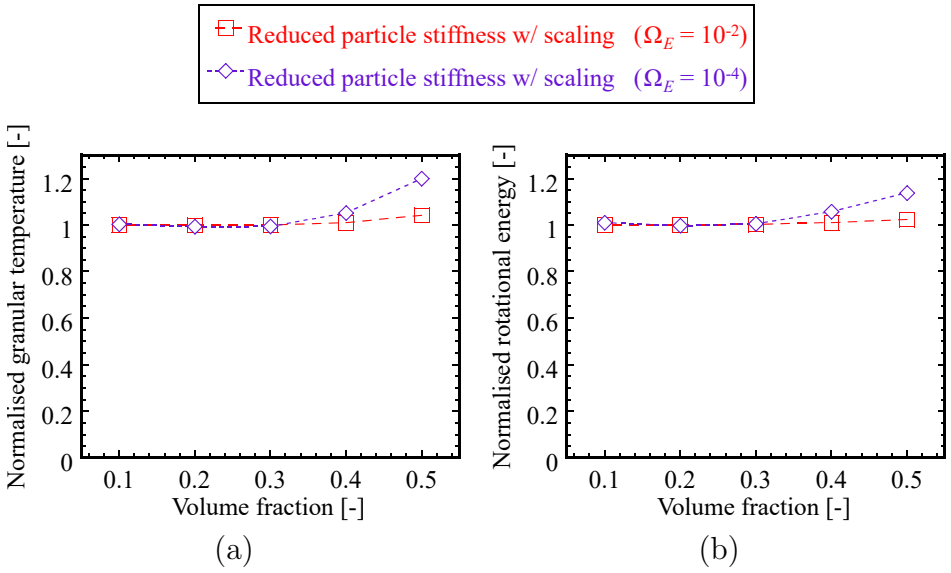

Figure 13: (a) Granular temperature and (b) rotational energy normalised with the results of original system.

5.2. Bi-dispersed particles

Since the RPS scaling is derived from generic governing equations as explained in Section 3, it is expected to be applicable not only to mono-

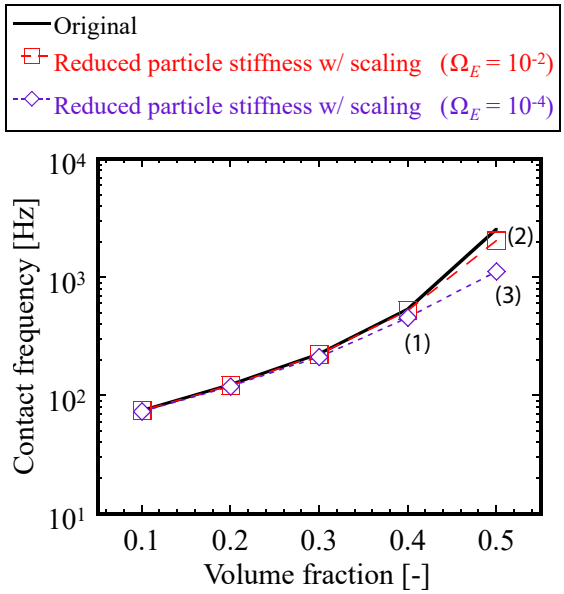

Figure 14: Average contact frequency in Couette flow. (1), (2) and (3) indicate the three conditions which have large deviation from the original system.

dispersed particles but also to mixtures of different particles. In this section, simulations of small and large particles with diameters of 1 and 2 mm, respectively, are presented. The simulations are performed with different mass ratio of large particles, C, from 0 to 1 as shown in Figure 15. The volume fraction used is $\phi = 0.4$ in all cases. The JKR and AR models are employed for the attraction force and rolling resistance, respectively, with a surface energy of 0.02 J/m^2 and maximum rotation angle of 0.01 rad. In the reduced system, the Young's modulus is reduced by 100 (i.e., $\Omega_E = 10^{-2}$).

Figures 16 and 17 show the results of the reduced systems with no scaling and the RPS scaling, respectively, plotted together with those of the original system. In Figure 16, the results of the original and reduced systems

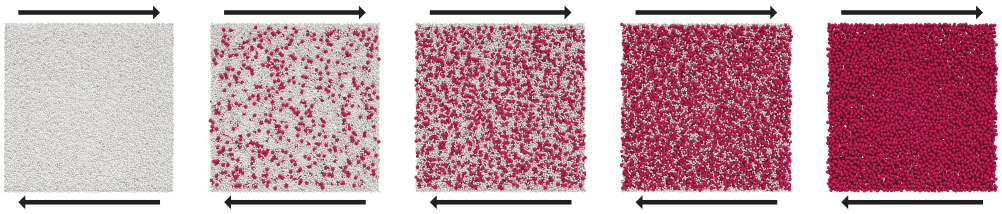

Figure 15: Snapshots of Couette flow of original mixtures of small particles (white) and large particles (red). The mass ratio of large particles is (a) 0, (b) 0.25, (c) 0.5, (d) 0.75 and (e) 1. The volume fraction used is 0.4.

are largely different in all cases, and similar discussion for Figure 12 in the previous section can be applied again: the particles become more cohesive and form large agglomerates and/or lumps when the stiffness is reduced. In Figure 17, it can be seen that the profiles of the average velocity and volume fraction are not affected by C except for the marginal difference in the near-wall region ($z/H < 0.2$ and $z/H > 0.8$). The granular temperature increases as the mass ratio increases until $C = 0.75$, and then it almost plateaus (Figure 17c). The rotational energy increases rather monotonically with increasing C (Figure 17d). These results are in good agreement with those of the original system. It is concluded that the RPS scaling is valid for poly-dispersed systems.

5.3. Effect of rolling resistance

According to Tables 3 and 4, it is necessary to scale both attraction force and rolling resistance in reduced systems if the JKR model is used with AR model. In literature, plenty of discussion can be found for attraction force scaling of the JKR model [39, 40, 46, 47], but only limited work properly

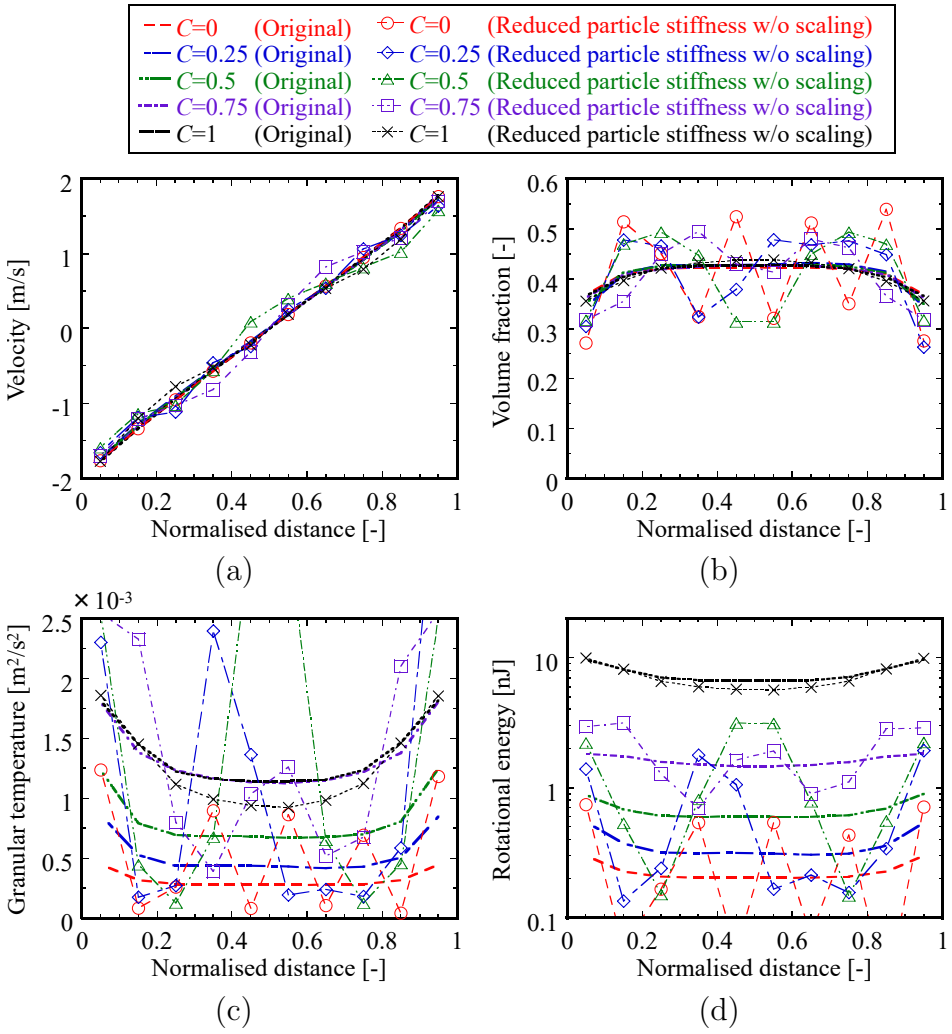

Figure 16: Time- and spatial-averaged quantities with different mass ratio of large particles (0, 0.25, 0.5, 0.75 and 1); (a) velocity, (b) volume fraction, (c) granular temperature and (d) rotational energy in steady state. The volume fraction is 0.4. $\Omega_E = 10^{-2}$ and no scaling is applied in the reduced system.

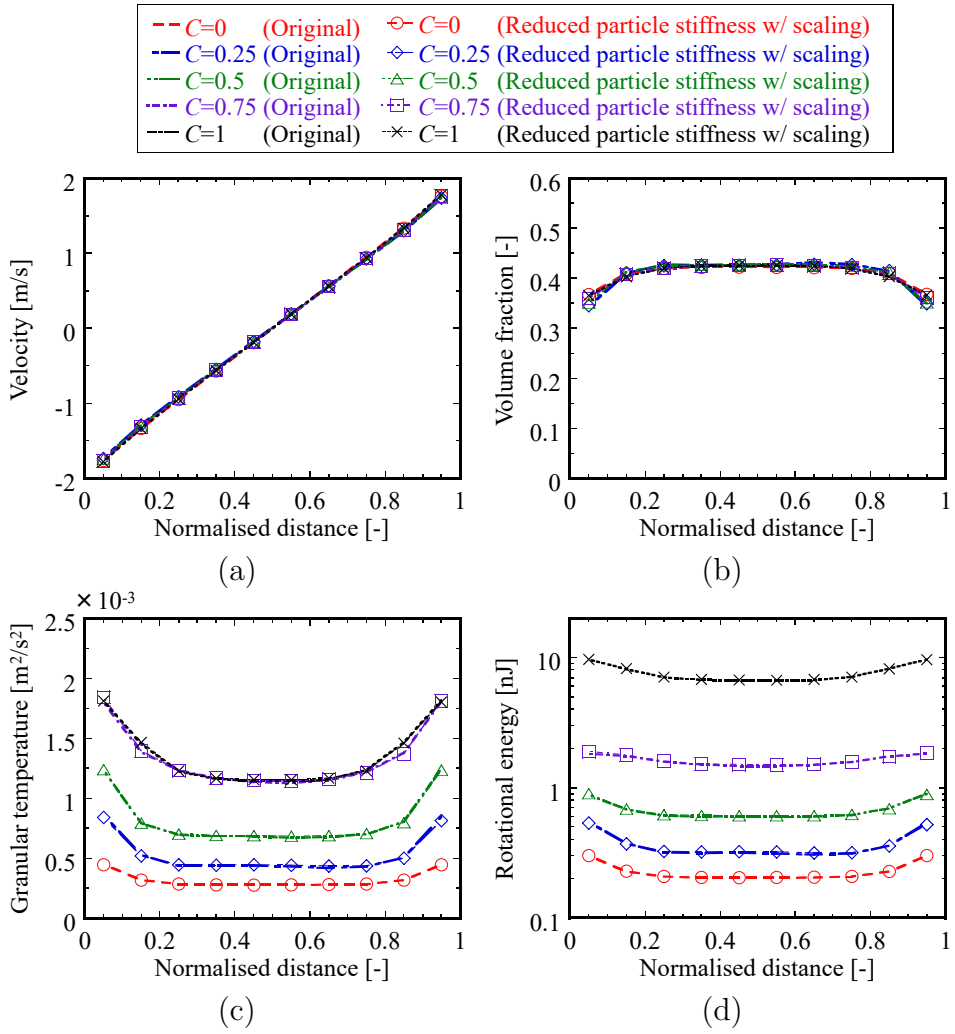

Figure 17: Time- and spatial-averaged quantities with different mass ratio of large particles (0, 0.25, 0.5, 0.75 and 1); (a) velocity, (b) volume fraction, (c) granular temperature and (d) rotational energy in steady state. The volume fraction is 0.4. $\Omega_E = 10^{-2}$ and the RPS scaling is applied in the reduced system.

discusses the rolling resistance scaling. In this section, the attraction force is artificially eliminated to focus on the effect of rolling resistance scaling of the AR model. In other words, the Hertzian model is used for contact force calculation, and the surface energy only contributes to the rolling resistance. The simulations are performed with different surface energies (0.1, 1 and 10 J/m^2) with maximum rotation angle of 0.01 rad. The particle diameter is given with the Gaussian distribution with a mean of 1 mm and standard deviation of 0.05 mm, and the volume fraction is $\phi = 0.4$ in all cases. In the reduced system, the Young's modulus is reduced by 100 (i.e., $\Omega_E = 10^{-2}$).

Figure 18 shows the profiles of the granular temperature and rotational energy. In the results of the reduced particle stiffness without any scaling, the granular temperature is slightly smaller than the original case especially in the high surface energy case ($\gamma = 10$ J/m^2), although the deviation is not significant. On the other hand, the rotational energy is retarded more drastically due to the increased net rolling torque. To the best of the authors' knowledge, this is the first time the effect of the rolling resistance is properly evaluated in a reduced system. The results of the original and reduced systems with the RPS scaling are almost identical, which proves the correctness of the theory developed in Section 3.

In many simulations in literature, the CDT and EPSD models are two popular choices for rolling resistance [21, 22, 23, 43] in DEM. Fortunately, no scaling is required for these models as shown in Tables 2 and 4. Some additional simulations have been performed to prove this point. The calcu-

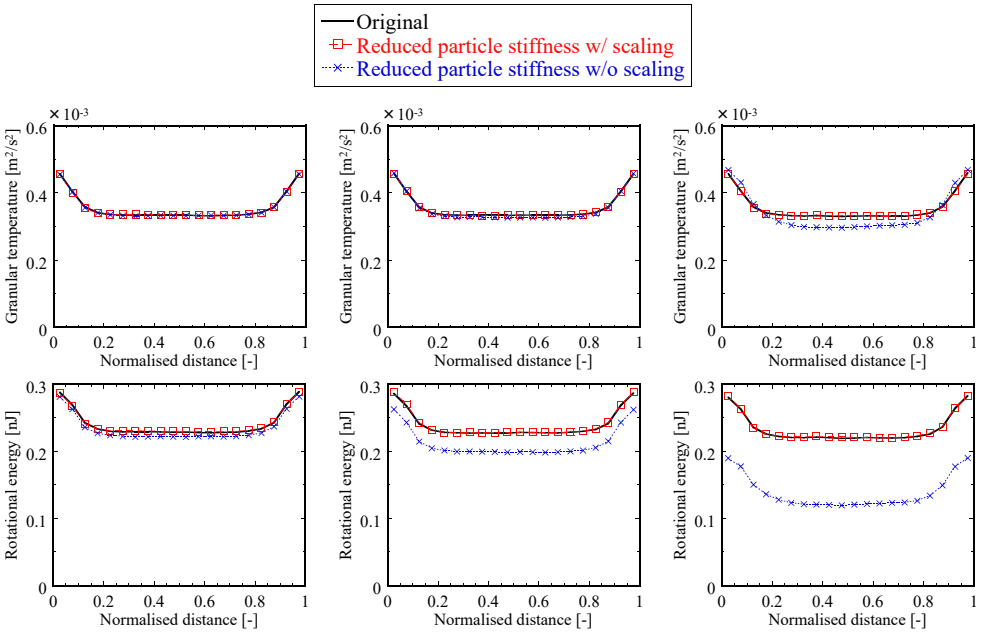

Figure 18: Time- and spatial-averaged granular temperature (top row) and rotational energy (bottom row) with the AR model at different surface energies. The surface energy only contributes to the rolling resistance. The volume fraction is 0.4. $\Omega_E = 10^{-2}$ in the reduced system.

lation conditions are the same as above (for Figure 18) except that the CDT model is used for the rolling resistance rather than the AR model (and hence the surface energy is not used anymore). The coefficient of rolling resistance used is $\mu_r = 0.1$. In the reduced system, the Young's modulus is reduced by 100 (i.e., $\Omega_E = 10^{-2}$).

Figure 19 shows the profiles of the granular temperature and rotational energy. The results of the original and reduced systems (without scaling) fall almost on the same curve as expected. Therefore, it can be said that the simulation results in the literature above appear to be reasonable in terms of the rolling resistance and stiffness reduction.

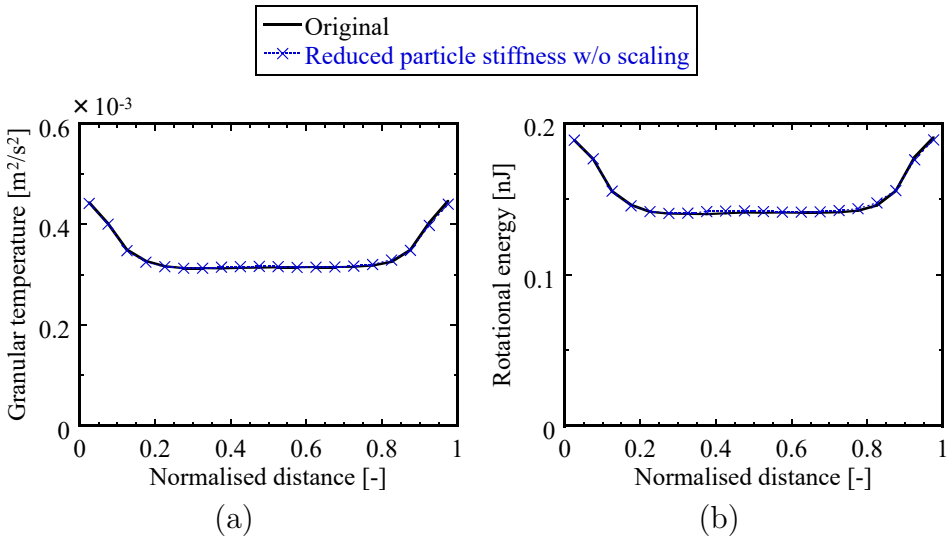

Figure 19: Profiles of time- and spatial-averaged (a) granular temperature and (b) rotational energy with the CDT model in steady state. $\Omega_E = 10^{-2}$ in the reduced system. The volume fraction is 0.4 and the coefficient of rolling resistance is 0.1.

6. Conclusions

In this work, an extended theory of the RPS scaling for DEM simulation is proposed. It provides generic scaling laws for attraction force and rolling resistance with reduced particle stiffness. The scaling laws are derived from the dimensionless equations of motion for both translation and rotation and with multi-body interactions. The resultant scaling laws can be used with any combinations of contact force, attraction force and rolling resistance. In the simulation of head-on collisions of three particles, it is verified that the RPS scaling can maintain the same particle motions in both translation and rotation in terms of the dimensionless time and space during contact. The following are the key findings from the validation simulations of Couette flow:

- It is proven that the RPS scaling can replicate the flow of the original system well in general, but some discrepancies can be observed when the solid fraction is high and/or the stiffness is largely reduced. It is inferred that the discrepancies are caused by the reduction of contact frequency.

- The RPS scaling is proven to be applicable for poly-dispersed systems.

- The reduction of particle stiffness can influence the results when the AR model for rolling resistance is used, and the RPS scaling can capture the particle rotation of the original system well.

- It is theoretically revealed for the first time that no scaling is required

for the CDT and EPSD models when used with reduced particle stiffness, which is often assumed in many pieces of work in literature.

Acknowledgements

The authors are grateful to Hosokawa Powder Technology Foundation for the financial support to this work. This research was supported in part through computational resources provided by Research Institute for Information Technology, Kyushu University.

References

[1] P. A. Cundall, O. D. L. Strack, A discrete numerical model for granular assemblies, Géotechnique 29 (1979) 47–65. doi:10.1680/geot.1979.29.1.47.
URL https://www.icevirtuallibrary.com/doi/10.1680/geot.1979.29.1.47

[2] Y. Tsuji, T. Kawaguchi, T. Tanaka, Discrete particle simulation of two-dimensional fluidized bed, Powder Technology 77 (1993) 79–87. doi:10.1016/0032-5910(93)85010-7.

[3] Y. Tsuji, T. Tanaka, T. Ishida, Lagrangian numerical simulation of plug flow of cohesionless particles in a horizontal pipe, Powder Technology 71 (1992) 239–250. doi:10.1016/0032-5910(92)88030-L.

[4] D. Antypov, J. A. Elliott, On an analytical solution for the damped hertzian spring, EPL 94 (2011) 50004. doi:10.1209/0295-5075/94/50004.

[5] T. Mikami, H. Kamiya, M. Horio, Numerical simulation of cohesive powder behavior in a fluidized bed, Chemical Engineering Science 53 (1998) 1927–1940. doi:10.1016/S0009-2509(97)00325-4.

[6] Y. Muguruma, T. Tanaka, Y. Tsuji, Numerical simulation of particulate flow with liquid bridge between particles (simulation of centrifugal tumbling granulator), Powder Technology 109 (2000) 49–57. doi:10.1016/S0032-5910(99)00226-0.
URL https://linkinghub.elsevier.com/retrieve/pii/S0032591099002260

[7] Y. I. Rabinovich, M. S. Esayanur, B. M. Moudgil, Capillary forces between two spheres with a fixed volume liquid bridge: Theory and experiment, Langmuir 21 (2005) 10992–10997. doi:10.1021/la0517639.

[8] P. Lambert, A. Chau, A. Delchambre, S. Régnier, Comparison between two capillary forces models, Langmuir 24 (2008) 3157–3163. doi:10.1021/la7036444.

[9] M. J. Adams, V. Perchard, The cohesive forces between particles with interstitial liquid, Institute of Chemical Engineering Symposium 91 (1985) 147–160.

[10] O. Pitois, P. Moucheront, X. Chateau, Liquid bridge between two moving spheres: An experimental study of viscosity effects, Journal of Colloid and Interface Science 231 (2000) 26–31. doi:10.1006/jcis.2000.7096.

[11] K. Washino, E. L. Chan, T. Matsumoto, S. Hashino, T. Tsuji, T. Tanaka, Normal viscous force of pendular liquid bridge between two relatively moving particles, Journal of Colloid and Interface Science 494 (2017) 255–265. doi:10.1016/j.jcis.2017.01.088.

[12] A. J. Goldman, R. G. Cox, H. Brenner, Slow viscous motion of a sphere parallel to a plane wall-i motion through a quiescent fluid, Chemical Engineering Science 22 (1967) 637–651. doi:10.1016/0009-2509(67)80047-2.

[13] K. Washino, E. L. Chan, H. Midou, T. Tsuji, T. Tanaka, Tangential viscous force models for pendular liquid bridge of newtonian fluid between moving particles, Chemical Engineering Science 174 (2017) 365–373. doi:10.1016/j.ces.2017.09.028.

[14] J. Yang, C. Y. Wu, M. Adams, Dem analysis of the effect of electrostatic interaction on particle mixing for carrier-based dry powder inhaler formulations, Particuology 23 (2015) 25–30. doi:10.1016/j.partic.2014.12.007.

[15] C. Pei, C. Y. Wu, M. Adams, Dem-cfd analysis of contact electrification and electrostatic interactions during fluidization, Powder Technology 304 (2016) 208–217. doi:10.1016/j.powtec.2016.08.030.

[16] K. L. Johnson, K. Kendal, A. D. Roberts, Surface energy and the contact of elastic solids, Proceedings of the Royal Society of Lon-

don. A. Mathematical and Physical Sciences 324 (1971) 301–313. doi:10.1098/rspa.1971.0141.

[17] B. V. Derjaguin, V. M. Muller, Y. P. Toporov, Effect of contact deformations on the adhesion of particles, Progress in Surface Science 45 (1994) 131–143. doi:10.1016/0079-6816(94)90044-2.

[18] D. Maugis, Adhesion of spheres: The jkr-dmt transition using a dugdale model, Journal of Colloid And Interface Science 150 (1992) 243–269. doi:10.1016/0021-9797(92)90285-T.

[19] B. K. Mishra, C. Thornton, Impact breakage of particle agglomerates, International Journal of Mineral Processing 61 (2001) 225–239. doi:10.1016/S0301-7516(00)00065-X.

[20] A. Hassanpour, S. J. Antony, M. Ghadiri, Effect of size ratio on the behaviour of agglomerates embedded in a bed of particles subjected to shearing: Dem analysis, Chemical Engineering Science 62 (2007) 935–942. doi:10.1016/j.ces.2006.10.026.

[21] Y. C. Zhou, B. D. Wright, R. Y. Yang, B. H. Xu, A. B. Yu, Rolling friction in the dynamic simulation of sandpile formation, Physica A: Statistical Mechanics and its Applications 269 (1999) 536–553. doi:10.1016/S0378-4371(99)00183-1.

[22] K. Iwashita, M. Oda, Rolling resistance at contacts in simulation of shear band development by dem, Journal of Engineering Mechanics

124 (1998) 285–292, doi: 10.1061/(ASCE)0733-9399(1998)124:3(285). doi:10.1061/(asce)0733-9399(1998)124:3(285).

[23] M. J. Jiang, H. S. Yu, D. Harris, A novel discrete model for granular material incorporating rolling resistance, Computers and Geotechnics 32 (2005) 340–357. doi:10.1016/j.compgeo.2005.05.001.

[24] C. Dominik, A. G. Tielens, Resistance to rolling in the adhesive contact of two elastic spheres, Philosophical Magazine A: Physics of Condensed Matter, Structure, Defects and Mechanical Properties 72 (1995) 783–803. doi:10.1080/01418619508243800.

[25] C. M. Wensrich, A. Katterfeld, Rolling friction as a technique for modelling particle shape in dem, Powder Technology 217 (2012) 409–417. doi:10.1016/j.powtec.2011.10.057.

[26] J. Ai, J. F. Chen, J. M. Rotter, J. Y. Ooi, Assessment of rolling resistance models in discrete element simulations, Powder Technology 206 (2011) 269–282. doi:10.1016/j.powtec.2010.09.030.

[27] T. Tsuji, K. Yabumoto, T. Tanaka, Spontaneous structures in three-dimensional bubbling gas-fluidized bed by parallel dem-cfd coupling simulation, Powder Technology 184 (2008) 132–140, cited By 92. doi:10.1016/j.powtec.2007.11.042.

[28] H. Mio, R. Higuchi, W. Ishimaru, A. Shimosaka, Y. Shirakawa, J. Hidaka, Effect of paddle rotational speed on particle mixing be-

havior in electrophotographic system by using parallel discrete element method, Advanced Powder Technology 20 (2009) 406–415. doi:10.1016/j.apt.2009.05.002.

[29] N. Govender, D. N. Wilke, C. Y. Wu, R. Rajamani, J. Khinast, B. J. Glasser, Large-scale gpu based dem modeling of mixing using irregularly shaped particles, Advanced Powder Technology 29 (2018) 2476–2490. doi:10.1016/j.apt.2018.06.028.

[30] Y. He, T. J. Evans, A. B. Yu, R. Y. Yang, A gpu-based dem for modelling large scale powder compaction with wide size distributions, Powder Technology 333 (2018) 219–228. doi:10.1016/j.powtec.2018.04.034.

[31] Y. He, F. Muller, A. Hassanpour, A. E. Bayly, A cpu-gpu cross-platform coupled cfd-dem approach for complex particle-fluid flows, Chemical Engineering Science 223 (2020) 115712. doi:10.1016/j.ces.2020.115712.

[32] M. Sakai, S. Koshizuka, Large-scale discrete element modeling in pneumatic conveying, Chemical Engineering Science 64 (2009) 533–539. doi:10.1016/j.ces.2008.10.003.

[33] M. Sakai, Y. Yamada, Y. Shigeto, K. Shibata, V. M. Kawasaki, S. Koshizuka, Large-scale discrete element modeling in a fluidized bed, International Journal for Numerical Methods in Fluids 64 (2010) 1319–1335. doi:10.1002/fld.2364.

[34] E. L. Chan, K. Washino, Coarse grain model for dem simulation of dense and dynamic particle flow with liquid bridge forces, Chemical Engineering Research and Design 132 (2018) 1060–1069. doi:10.1016/j.cherd.2017.12.033.

[35] K. Washino, E. L. Chan, T. Kaji, Y. Matsuno, T. Tanaka, On large scale cfd–dem simulation for gas–liquid–solid three-phase flows, Particuology 59 (2021) 2–15. doi:10.1016/j.partic.2020.05.006.
URL https://linkinghub.elsevier.com/retrieve/pii/S1674200120300754

[36] K. Washino, E. L. Chan, Y. Nishida, T. Tsuji, Coarse grained dem simulation of non-spherical and poly-dispersed particles using scaled-up particle (sup) model, Powder Technology 426 (2023) 118676. doi:10.1016/j.powtec.2023.118676.
URL https://linkinghub.elsevier.com/retrieve/pii/S0032591023004606

[37] Z. Yan, S. K. Wilkinson, E. H. Stitt, M. Marigo, Discrete element modelling (dem) input parameters: understanding their impact on model predictions using statistical analysis, Computational Particle Mechanics 2 (2015) 283–299. doi:10.1007/s40571-015-0056-5.

[38] T. Kobayashi, T. Tanaka, N. Shimada, T. Kawaguchi, Dem-cfd analysis of fluidization behavior of geldart group a particles using a dynamic adhesion force model, Powder Technology 248 (2013) 143–152. doi:10.1016/j.powtec.2013.02.028.

[39] J. Hærvig, U. Kleinhans, C. Wieland, H. Spliethoff, A. Jensen, K. Sørensen, T. Condra, On the adhesive jkr contact and rolling models for reduced particle stiffness discrete element simulations, Powder Technology 319 (2017) 472–482. doi:10.1016/j.powtec.2017.07.006.
URL https://linkinghub.elsevier.com/retrieve/pii/S0032591017305430

[40] Y. He, A. Hassanpour, M. A. Behjani, A. E. Bayly, A novel stiffness scaling methodology for discrete element modelling of cohesive fine powders, Applied Mathematical Modelling 90 (2021) 817–844. doi:10.1016/j.apm.2020.08.062.

[41] Y. Li, Y. Xu, C. Thornton, A comparison of discrete element simulations and experiments for 'sandpiles' composed of spherical particles, Powder Technology 160 (2005) 219–228. doi:10.1016/j.powtec.2005.09.002.

[42] H. P. Kuo, P. C. Knight, D. J. Parker, Y. Tsuji, M. J. Adams, J. P. Seville, The influence of dem simulation parameters on the particle behaviour in a v-mixer, Chemical Engineering Science 57 (2002) 3621–3638. doi:10.1016/S0009-2509(02)00086-6.

[43] S. Miyai, M. Kobayakawa, T. Tsuji, T. Tanaka, Influence of particle size on vertical plate penetration into dense cohesionless granular materials (large-scale dem simulation using real particle size), Granular Matter 21. doi:10.1007/s10035-019-0961-z.

[44] R. L. Stewart, J. Bridgwater, Y. C. Zhou, A. B. Yu, Simulated and

measured flow of granules in a bladed mixer- a detailed comparison, Chemical Engineering Science 56 (2001) 5457–5471. doi:10.1016/S0009-2509(01)00190-7.

[45] E. L. Chan, K. Washino, G. K. Reynolds, B. Gururajan, M. J. Hounslow, A. D. Salman, Blade-granule bed stress in a cylindrical high shear granulator: Further characterisation using dem, Powder Technology 300 (2016) 92–106. doi:10.1016/j.powtec.2016.02.010.

[46] K. Washino, E. L. Chan, T. Tanaka, Dem with attraction forces using reduced particle stiffness, Powder Technology 325 (2018) 202–208. doi:10.1016/j.powtec.2017.11.024.

[47] S. Chen, W. Liu, S. Li, A fast adhesive discrete element method for random packings of fine particles, Chemical Engineering Science 193 (2019) 336–345. doi:10.1016/j.ces.2018.09.026.

[48] E. J. Parteli, J. Schmidt, C. Blümel, K. E. Wirth, W. Peukert, T. Pöschel, Attractive particle interaction forces and packing density of fine glass powders, Scientific Reports 4 (2014) 1–7. doi:10.1038/srep06227.

[49] C. Thornton, Interparticle sliding in the presence of adhesion, Journal of Physics D: Applied Physics 24 (1991) 1942–1946. doi:10.1088/0022-3727/24/11/007.

[50] J. S. Marshall, Discrete-element modeling of particulate aerosol flows, Journal of Computational Physics 228 (2009) 1541–1561. doi:10.1016/j.jcp.2008.10.035.

[51] K. Washino, E. L. Chan, K. Miyazaki, T. Tsuji, T. Tanaka, Time step criteria in dem simulation of wet particles in viscosity dominant systems, Powder Technology 302 (2016) 100–107. doi:10.1016/j.powtec.2016.08.018.

[52] D. Tabor, Surface forces and surface interactions, Journal of Colloid And Interface Science 58 (1977) 2–13. doi:10.1016/0021-9797(77)90366-6.

[53] C. Goniva, C. Kloss, N. G. Deen, J. A. Kuipers, S. Pirker, Influence of rolling friction on single spout fluidized bed simulation, Particuology 10 (2012) 582–591. doi:10.1016/j.partic.2012.05.002.

[54] C. Dominik, A. G. G. M. Tielens, The physics of dust coagulation and the structure of dust aggregates in space, The Astrophysical Journal 480 (1997) 647–673. doi:10.1086/303996.

[55] G. Q. Liu, J. S. Marshall, Effect of particle adhesion and interactions on motion by traveling waves on an electric curtain, Journal of Electrostatics 68 (2010) 179–189. doi:10.1016/j.elstat.2009.12.007.

[56] B. Sümer, M. Sitti, Rolling and spinning friction characterization of fine particles using lateral force microscopy based contact push-

ing, Journal of Adhesion Science and Technology 22 (2008) 481–506. doi:10.1163/156856108X295527.

[57] K. Samiei, B. Peters, M. Bolten, A. Frommer, Assessment of the potentials of implicit integration method in discrete element modelling of granular matter, Computers and Chemical Engineering 49 (2013) 183–193. doi:10.1016/j.compchemeng.2012.10.009.

[58] C. S. Campbell, Boundary interactions for two-dimensional granular flows. part 1. flat boundaries, asymmetric stresses and couple stresses, Journal of Fluid Mechanics 247 (1993) 111–136. doi:10.1017/S0022112093000400.